De novo design of potent and selective mimics of IL-2 and IL-15

Daniel-Adriano Silva[1,2,*,&], **Shawn Yu**[1,3,*], **Umut Ulge**[1,3,*], **Jamie B. Spangler**[4,*], **Kevin M. Jude**[5], **Carlos Labão-Almeida**[6], **Lestat R. Ali**[7], **Alfredo Quijano-Rubio**[1,2,3], **Mikel Ruterbusch**[8], **Isabel Leung**[9], **Tamara Biary**[7], **Stephanie J. Crowley**[7], **Enrique Marcos**[10], **Carl D. Walkey**[1,2], **Brian D. Weitzner**[1,2], **Fátima Pardo-Avila**[11], **Javier Castellanos**[1,2,§], **Lauren Carter**[1], **Lance Stewart**[1], **Stanley Riddell**[9], **Marion Pepper**[8], **Gonçalo J. L. Bernardes**[6,12], **Michael Dougan**[7], **K. Christopher Garcia**[5,13,&], and **David Baker**[1,2,13,&]

[1.]Institute for Protein Design, University of Washington, Seattle, WA 98195, USA.

[2.]Department of Biochemistry, University of Washington, Seattle, WA 98195, USA.

[3.]Department of Bioengineering, University of Washington, Seattle, WA 98195, USA.

[4.]Chemical and Biomolecular Engineering, Johns Hopkins, Baltimore, MD 21205, USA.

[5.]Departments of Molecular and Cellular Physiology and Structural Biology, Stanford University School of Medicine, Stanford, CA 94305, USA.

[6.]Instituto de Medicina Molecular, Faculdade de Medicina, Universidade de Lisboa, Avenida Professor Egas Moniz, 1649-028, Lisboa, Portugal.

[7.]Division of Gastroenterology, Massachusetts General Hospital, Boston, MA 02114, USA.

[8.]Department of Immunology, University of Washington School of Medicine, Seattle, WA 98109, USA.

[9.]Fred Hutchinson Cancer Research Center, Clinical Research Division, 1100 Fairview Ave. North, Seattle, WA 98109, USA.

& Corresponding authors. Mail to: dadriano@uw.edu, kcgarcia@stanford.edu or dabaker@uw.edu.
§ Present address: Cyrus Biotechnology, 500 Union St, suite 320, Seattle, WA, 98101.

Author Manuscript

[10.]Institute for Research in Biomedicine (IRB Barcelona), The Barcelona Institute of Science and Technology, Baldiri Reixac 10, 08028 Barcelona, Spain.

[11.]Department of Structural Biology, Stanford University School of Medicine, Stanford, CA 94305, USA.

[12.]Department of Chemistry, University of Cambridge, Lensfield Road, Cambridge CB2 1EW, UK.

[13]Howard Hughes Medical Institute

Keywords

De novo; protein; design; functional; hyper-stable; cytokine; interleukin-2; interleukin-15; il-2; il-15; mimic; mimetic; therapeutic; cancer; Neoleukin; Neoleukin-2/15; Neo-2/15

We describe a *de novo* computational approach for designing proteins that recapitulate the functional sites of natural signaling proteins, but otherwise are unrelated in topology or amino acid sequence. We use this strategy to design mimics of the central immune cytokine interleukin-2 (IL-2) that bind to the IL-2 receptor $\beta\gamma_c$ heterodimer (IL-2R$\beta\gamma_c$), but have no binding site for IL-2Rα or IL-15Rα. The designs are hyper-stable, bind human and mouse IL-2R$\beta\gamma_c$ with higher affinity than the natural cytokines, and elicit downstream cell signaling independent of IL-2Rα and IL-15Rα. Crystal structures of Neoleukin-2/15 (Neo-2/15), an experimentally optimized mimic, are very close to the designed model. Neo-2/15 has superior therapeutic activity than IL-2 in murine models of melanoma and colon cancer, with reduced toxicity and undetectable immunogenicity. Our strategy for building hyper-stable *de novo* mimetics can be applied to signaling proteins quite generally, enabling the creation of superior therapeutic candidates.

The considerable potential of the central immune cytokine interleukin-2 (IL-2) for cancer treatment[1–3] has sparked numerous efforts to improve its therapeutic properties by mutation and/or chemical modification[4–11]. Such efforts have sought to simplify manufacturing, extend half-life, and modulate receptor interactions[12–14]. However, there are inherent challenges to the development of a new therapeutic when starting with a naturally occurring bioactive protein. First, most natural proteins are only marginally stable[15–17], hence amino acid substitutions aimed at increasing efficacy can decrease expression or cause aggregation, making manufacturing and storage difficult. More substantial changes, such as the deletion or fusion of functional or targeting domains, are often unworkable and can dramatically alter pharmacokinetic properties and tissue penetration[13]. Second, any immune response against the engineered variant may cross-react with the endogenous molecule[18–24] with potentially catastrophic consequences. Third, the target receptor subunit interaction profile can be difficult to reprogram. The clinical use of IL-2 has been mainly limited by toxicity[25–27] which, while incompletely understood in humans, is T cell independent in murine models and considerably reduced in animals deficient in the IL-2Rα chain (CD25$^-$). Previous efforts at removing the CD25 interaction region in IL-2 and its reengineered variants, by either mutation[5,8,28,29] (e.g. Super-2) or PEGylation (e.g. NKTR-214[11]), have resulted in markedly reduced stability, binding and/or potency of the cytokine while failing to completely eliminate the interaction with CD25. Here, we sought to develop a computational design

approach to generate analogs of natural proteins with improved therapeutic properties that circumvent these challenges, focusing our effort on engineering *de novo* cytokine mimics displaying the specific receptor binding interfaces optimal for treating disease.

Computational design of IL-2/IL-15 mimics that bind and activate IL-2Rβγ$_c$:

Cytokines interact with multiple receptor subunits[30–33], and like most naturally occurring proteins, contain non-ideal structural features that compromise its stability but are important for function. We developed a computational protocol in which the structural elements interacting with the desired receptor subunit(s) are fixed in space (Fig. 1a), and an idealized globular protein structure is built to support these elements. *De novo* design has been used previously to support short linear epitopes[34–37]; here we support more complex binding interfaces by using a parametric construction of disembodied helices coupled with knowledge-based loop closure[38] (Fig. 1b–c). We tested our approach by attempting to *de novo* design stable idealized proteins with interaction surfaces mimicking those of human IL-2 (hIL-2) and human IL-15 (hIL-15) for the human IL-2Rβγ$_c$ (hIL-2Rβγ$_c$)[32,39], but entirely lacking the alpha (CD25) receptor interaction surface.

Native hIL-2 comprises four helices (Fig. 1a) connected by long irregular loops. The N-terminal helix (H1) interacts with both the beta and gamma subunits, the third helix (H3) interacts with the beta subunit, and the C-terminal helix (H4) with the gamma subunit; the alpha subunit interacting surface is formed by the irregular second helix (H2) and two long loops, one connecting H1 to H2 and the other connecting H3 and H4. We aimed to build an idealized protein that recapitulates the interface formed by H1, H3, and H4 with beta and gamma and to replace H2 with a helix that offers better packing and ignores the interaction with the alpha subunit. Two generations of designed mimics were made. In a first generation, we used all helices (H1, H2, H3, and H4) from hIL-2 (Fig. 1a) as starting points for structure idealization by (independently) rebuilding each disembodied helix using commonly occurring protein fragments (see Methods), and connecting helices with fragment derived loops (Fig. 1c) to generate fully connected backbones (Fig. 1d). For each backbone (in complex with hIL-2Rβγ$_c$) Rosetta combinatorial flexible backbone sequence design was carried out[40–42] resulting in a considerably more regular structure for H2 (H2') than in hIL-2 (Fig. 1b, top panel; see Methods). The four lowest energy designs and eight single-disulfide stapled variations (SI Table S1) were selected for experimental characterization by yeast display (see Methods). Eight designs bound fluorescently-tagged beta-gamma chimeric IL-2 receptor at low-nanomolar concentrations (SI Fig. S1), and the highest affinity non-disulfide design (G1_neo2_40) was subjected to site-saturation mutagenesis (SI Table S5), followed by a library of combinatorial substitutions (enriched in selections against hIL-2Rβγ$_c$, SI Fig. S2 and Table S7). The highest affinity variants (SI Fig. S4 and SI Table S2) were expressed recombinantly in *E. coli* and found to elicit pSTAT5 signaling *in vitro* on IL-2-responsive murine cells at low-nanomolar or even picomolar concentrations (Table E1), but had relatively low thermal stability (Tm ~<45°C, SI Figs. S3 and S5). To improve stability, in a second generation of designs, we repeated the computational design protocol starting from the backbone of the highest affinity first-round design (G1_neo2_40_1F, topology: H1->H4->H2'->H3), but this time coupling the loop building process with parametric variation of the helix lengths (+/− 8 amino acids, Fig. 1b bottom panel). This second generation approach

improved the quality of the models by enabling the exploration of substantially more combinations of high-quality loops connecting each pair of helices. The fourteen-second generation designs with highest predicted affinity and stability, along with twenty-seven Rosetta sequence redesigns of G1_neo2_40_1F (SI Table S3), were experimentally characterized and all but one were found to bind the hIL-2 receptor at low-nanomolar concentrations (Fig. 1f, extended Table E1, and SI Fig. S6). The three highest affinity and stability designs (one sequence redesign and two new mimetics) were subjected to site-saturation mutagenesis (SI Table S6), followed by combinatorial libraries of substitutions increasing affinity against mIL-2Rβγ$_c$ (SI Figs. S8–10 and Tables S6 and S8), which yielded higher affinity hyper-stable variants of the *de novo* mimics (extended Table E1, SI Tables S4 and S8, and SI Figs. S11–13). The second generation optimized design with highest overall affinity for both human and mouse IL-2Rβγ$_c$, Neoleukin-2/15, is a 100-residue protein with a new topology and sequence quite different from human or murine IL-2 (BLASTP sequence identity to hIL-2 and mIL-2 of 14% and 24% respectively; MICAN structural-based sequence identity to hIL-2 and mIL-2 of 29% and 16% respectively, see Methods and extended Table E1).

Functional characterization of Neo-2/15:

Neo-2/15 binds with high affinity to human and mouse IL-2Rβγ$_c$ (Kd ~19 nM and ~38, respectively) but does not interact with IL-2Rα (Fig. 2a). The affinities of Neo-2/15 for the human and mouse IL-2 receptors (IL-2Rβ and IL-2Rβγ$_c$) are significantly higher than those of the corresponding native IL-2 cytokines (Table E1). Neo-2/15 activates IL-2Rα$^-$ human YT-1 cells more potently than native hIL-2 (EC$_{50}$ = 49 pM vs. 410 pM) and IL-2Rα$^-$ mouse primary T cells more potently than native mIL-2 (EC$_{50}$ = 130 pM vs. 30 nM), which is consistent with its higher binding affinity (Fig. 2b, SI Table S9). Neo-2/15 is more active than Super-2 on IL-2Rα$^-$ mouse primary T cells (EC$_{50}$ = 130 pM vs. 660 pM) and less active than Super-2 on IL-2Rα$^+$ cells (EC$_{50}$ = 24 pM vs. 1.2 pM), presumably due to its complete lack of IL-2Rα binding (Fig. 2b). Neo-2/15 is hyper-stable (SI Fig. S13) and does not lose binding affinity for hIL-2Rβγ$_c$ following incubation at 80°C for 2 hours, while hIL-2 and Super-2 are completely inactivated after 10 minutes (half-inactivation time = ~4.2 min and ~2.6 min, respectively, Fig. 2c, top panel). In *ex vivo* primary cell cultures, Neo-2/15 drives T cell survival effectively after 60 minutes of boiling at 95°C, whereas these conditions inactivated both IL-2 and Super-2 (Fig. 2c, bottom panel). This unprecedented stability for a cytokine-like molecule, beyond eliminating the requirement for cold chain storage, suggests a robustness to mutations (extended Fig. E8), genetic fusions and chemical modification (SI Fig. S14) greatly exceeding that of native IL-2, which could contribute to the development of improved or new therapeutic properties (extended Figs. E3–4).

Structure of monomeric Neo-2/15 and ternary complex with mIL-2Rβγ$_c$:

The X-ray crystal structure of Neo-2/15 is very close to the computational design model (r.m.s.d.$_{Cα}$ = 1.1–1.3 Å for the 6 copies in the asymmetric unit, Fig. 3a). Neo-2/15 enabled the determination of the previously unsolved murine IL-2Rβγ$_c$ complex, its structure aligns very closely to the previously reported human IL-2 receptor complex[43] (Fig. 3b, Table E2). The Neo-2/15 design model and its crystal structure align with the mouse ternary complex

structure with an r.m.s.d.$_{C\alpha}$ of 1.27 and 1.29 Å, respectively (Fig. 3c). The order of helices in Neo-2/15 (in IL-2 numbering) is H1->H3->H2'->H4 (Figs. 1a and 3a,d). The H1-H3 loop is disordered in the ternary complex, but helix H3 is in close agreement with the predicted structure; there is also an outward movement of helix H4 and the H2'-H4 loop compared to the monomeric structure (Fig. 3c). Neo-2/15 interacts with mIL-2Rβ via helices H1 and H3, and with γ_c via the H1 and H4 helices (Fig. 3); these regions align closely with both the computational design model (Fig. 3a) and the monomeric crystal structure (Fig. 3c). A ~4.0 Å shift for helix H4 (see Figure 3c) in the mouse complex may reflect the optimization for high-affinity binding to both the mouse and human receptors; Neo-2/15 design was based on the human complex structure and simulations suggest that there is little or no helix shift in this complex (see extended Fig. E7). Consistent with this, the helices of apo-Neo-2/15 superimpose closely on those of hIL-2 in complex with the human receptor (Fig. 3e–f), despite the different topology of the two proteins (Fig. 3d).

Therapeutic applications of Neo-2/15:

The inherent low stability of IL-2 and its tightly evolved dependence on CD25 have been barriers to the clinical translation of reengineered IL-2 compounds. Other efforts have focused on IL-15[44], since it elicits similar signaling to IL-2 by dimerizing the IL-2Rβγ_c but has no affinity for CD25. However, IL-15 activity is dependent on trans presentation of the IL-15α (CD215) receptor that is displayed primarily on antigen-presenting cells and NK cells. The low stability of native IL-15 and its dependence on trans presentation have also been substantial barriers to reengineering efforts[44,45].

Dose escalation studies on naive mice show that Neo-2/15 expands immunosuppressive Treg cells (T$_{reg}$) less than mIL-2 (Fig. 4a, left panel), leading to a higher CD8+ killer T cell : T$_{reg}$ ratio for Neo-2/15 than for mIL-2 (Fig. 4a, right panel). The increased expansion of regulatory T cells by mIL-2 is expected because mIL-2 binds preferentially to CD25+ cells[35,46,47]. The higher CD8 T cell : T$_{reg}$ ratios achieved with Neo-2/15 are generally associated with better tumor killing[8,11,29]; this functional advantage of Neo-2/15 likely stems from its higher affinity for IL-2βγ_c and lack of bias towards CD25+ cells. Similarly, in a murine model of airway inflammation that normally induces a small percentage of tissue-resident CD8+ T cells (Thy1.2- CD44+ CD8+), Neo-2/15 elicits an increase in the population of tissue-resident CD8+ T cells without increasing the population of antigen-specific T$_{reg}$ (CD4+ Foxp3+, Fig. 4b).

To test whether Neo-2/15 is immunogenic, naive and tumor-bearing mice were treated with Neo-2/15 daily (over a period of 4-weeks and 2-weeks, respectively). Little or no immunogenicity was observed in either case (Fig. 4c and extended Fig. E5); a similar lack of immune response has been observed for other *de novo* designed therapeutic candidates (likely due to their small size and high stability)[35]. Polyclonal antibodies against Neo-2/15 were generated by vaccinating mice with an inactive Neo-2/15 mutant (K.O. Neo-2/15) in complete Freund's adjuvant; importantly, these polyclonal (pAb) anti-Neo-2/15 antibodies do not cross-react with human or murine IL-2 (Fig. 4c and extended Fig. E5). Thus, even if there is an immune response to Neo-2/15 in a therapeutic setting, this response is unlikely to cross-react with endogenous IL-2. The low sequence identity between Neo-2/15 and hIL-2

(Table E1) makes an autoimmune response against host IL-2 much less likely for Neo-2/15 than for previously engineered hIL-2 variants (e.g. Super-2 or PEGylated variants of hIL-2), which differ from endogenous hIL-2 by only a few mutations (the BLASTP sequence identities of Neo2–15 and Super-2 to hIL-2 are 14% and 95%, respectively).

We tested the therapeutic efficacy of Neo-2/15 in B16F10 (melanoma) and CT26 (colon cancer) mouse models. Single-agent treatment with Neo-2/15 led to dose-dependent delays in tumor growth in both cancer models. In CT26 colon cancer, single agent treatment showed improved efficacy compared to mIL-2 (Fig. 4d and extended Fig. E1). In B16F10 melanoma, previous studies have shown that single-agent treatment with IL-2 is only partially effective, and co-treatment with the anti-melanoma cell antibody TA99 (anti-TRP1 mAb) is synergistic with IL-2[5,12,14] and IL-15 (superagonist complex ALT-803)[48]. In long-term survival experiments (8 weeks), Neo-2/15 in combination with TA99 showed substantially reduced toxicity and an overall superior therapeutic effect compared to mIL-2 (Fig. 4e extended Fig. E2), while treatment with TA99 alone has little effect. Mice treated with the combination mIL-2 and TA99 steadily lost weight and their overall health declined to the point of requiring euthanasia, whereas little decline was observed with the combination of Neo-2/15 and TA99 (Fig. 4e). Consistent with a therapeutic benefit, Neo-2/15 treatment led to a significant increase in intratumoral CD8:T_{reg} ratios (Fig. 4f and extended Fig. E1), which correlate with effective antitumor immune responses[49]. The increases of CD8:T_{reg} ratios by Neo-2/15 are dose- and antigen-dependent (Fig. 4f), which is consistent with the better therapeutic effects observed at higher doses and in combination with TA99 (extended Fig. E2). Altogether, these data show that Neo-2/15 exhibits the predicted homeostatic benefit derived from its IL-2-like immunostimulatory activity, but without the adverse effects associated with a $CD25^+$ preferential binding. These enhanced properties and low toxicity may allow the routine use of Neo-2/15 for indications for which IL-2 is not broadly used, such as to enhance CAR-T cell therapies (extended Fig. E4). The considerable activation of pSTAT5 signaling in naive mouse peripheral blood lymphocytes (CD8 and B cells) observed an hour after exposure to Neo-2/15 was much reduced after three hours (extended Fig. E6), suggesting that the efficacy of Neo-2/15 can likely be increased using standard approaches for extending circulation half-life, for example PEGylation[50].

De novo design of protein mimetics has the potential to transform the field of protein-based therapeutics, enabling the development of bio-superior molecules with enhanced therapeutic properties and reduced side-effects, not only for cytokines but for virtually any biologically active molecule with known or accurately predictable structure. Because of the incremental nature of current traditional engineering approaches (e.g. 1–3 amino acid substitutions, chemical modification at a single site), most of the shortcomings of the parent molecule are inevitably passed on to the resulting engineered variants, often in an exacerbated form. By building mimics completely from scratch, these shortcomings can be avoided: unlike recombinant IL-2 and its engineered variants, Neo-2/15 is well expressed in E. coli (SI Fig. S13), retains activity at high temperature, does not interact with IL-2Rα, and is robust to substantial sequence changes (extended Fig. E8) that can allow the engineering of new functions. Likely because of the small size and high stability of *de novo* designed proteins, immunogenicity appears to be low[35], and in contrast to incremental variants of hIL-2, any

antibody response mounted against mimetics is unlikely to cross-react with the natural parent cytokine. Because of their high stability and robustness, along with their tailored interaction surfaces, designed *de novo* protein mimetics are likely to be particularly powerful for developing next-generation therapeutics that combine different protein functionalities.

Methods

Computational design of de novo cytokine mimetics:

The design of *de novo* cytokine mimetics began by defining the structure of hIL-2 in the quaternary complex with the IL-2Rβγ$_c$ receptor as the template for the design. After inspection, the residues composing the binding-site were defined as hotspots using Rosetta's metadata (PDBInfoLabels). The structure was fed into the new mimetic design protocol that is programmed in PyRosetta, which can automatically detect the core-secondary structure elements that compose the target-template and produce the resulting de novo mimetic backbones with full RosettaScripts compatible information for design. Briefly, the mimetic building algorithm works as follows. For the first generation of designs, each of the core-elements was idealized by reconstruction using loops from a clustered database of highly-ideal fragments (fragment-size 4 amino acids, see Data availability). After idealization, the mimetic building protocol aims to reconnect the idealized elements by pairs in all possible combinations. To do this it uses combinatorial fragment assembly of sequence-agnostic fragments from the database, followed by cartesian-constrained backbone minimization for potential solutions (i.e. where the N- and C- ends of the built fragment are close enough to link the two secondary structures). After minimization, the solutions are verified to contain highly ideal fragments (i.e. that every overlapping fragment that composes the two connected elements is also contained within the database) and that no backbone clashes with the target (context) receptor. Successful solutions were then profiled using the same database of fragments in order to determine the most probable amino acids at each position (this information was encoded as metadata on each design). Next, solutions for pairs of connected secondary structures were combinatorially recombined (by using graph theory connected components) to produce fully connected backbones. Since the number of solutions grows exponentially with each pair of elements, at each fragment combination step we ranked the designs to favor those with shorter interconnections between pairs of secondary-structure core elements (i.e. effectively with shorter loops), and kept only the top solutions. Fully connected backbone solutions were profiled by layer (interface, core, non-core-surface, surface) in order to restrict the identities of the possible amino acids to be layer-compatible. Finally, all the information on hotspots, compatible built-fragment amino acids and layers were combined (hotspot has precedence to amino acid probability, and amino acid probability took precedence to layer). These fully profiled backbones were then passed to RosettaScripts for flexible backbone design and filtering (see SI Appendix A). For the second generation of designs, we followed two approaches. In the first approach, we just simply executed Rosetta sequence redesigns of our best first generation optimized design (G1_neo2_40_1F, SI Appendix B). In the second approach, we engineered new mimetics using G1_neo2_40_1F as the target template. The mimetic design protocol in this second generation was similar to the one described for the first generation, but with two key differences. Firstly, the core-elements (i.e. those that are secondary structures) were no

longer built from fragments, but instead by discovering parametric equations of repetitive phi and psi angles (omega fixed to 180°) that result in secondary structures that recapitulated each of the target helices as close as possible, a "pitch" on the phi and psi angles was allowed every 3rd residue in order to allow the helices the possibility to have curvature (final angle parameters: H1: phi=−60.4, psi=−45.8, phi_pitch=−1.0, psi_pitch=2.0; H2: phi=−64.5, psi=−38.4, phi_pitch=4.0, psi_pitch=−8.0; H3: phi=−64.6, psi=−40.6, phi_pitch=0.0, psi_pitch=0.0; H4: phi=−64.3, psi=−41.7, phi_pitch=0.0, psi_pitch=0.0). By using these parametric equations, the algorithm can variate the length of each of the core-elements up to ∓8.a.a. (compared to input the template). Reductions in the size of the core elements were not allowed to remove hotspots from the binding site. All length variations of the core-elements were reconnected with loops from a clustered database of highly ideal loops (fragment-size of 7 amino acids). The rest of the design algorithm was in essence similar to the one followed in the generation one (SI Appendix C). The Rosetta energy functions used for sequence design were "talaris2013" and "talaris2014", for the first and second generation of designs, respectively.

The databases of highly ideal fragments used for the design of the backbones for the *de novo* mimetics (see Data availability) were constructed with the Rosetta application "kcenters_clustering_of_fragments" using an extensive database of non-redundant (publicly available) protein structures from the RCSB protein data bank, which was comprised of 16767 PDBs for the 4-mer database (first generation of designs), and 7062 PDBs for the 7-mer database used for the second generation designs (see Data Availability). The computational algorithms for designing *de novo* mimics are also provided (see Data Availability).

Yeast display:

Yeast were transformed with genes encoding the proteins to be displayed together with a linearized pETcon3 vector. The vector was linearized by 100 fold overdigestion by NdeI and XhoI (New England Biolabs) and then purified by gel extraction (Qiagen). The genes included 50 bases of overlap with the vector on both the 5' and 3' end such that homologous recombination would place the genes in-frame between the AGA2 gene and the Myc tag on the vector. Yeast was grown in C-Trp-Ura media prior to induction in SGCAA media as previously described[34,35,51]. After induction for 12–18 hours, cells were washed in chilled display buffer (50mM NaPO$_4$ pH 8, 20mM NaCl, 0.5% BSA) and incubated with varying concentrations of biotinylated receptor (either human or murine IL-2Rα, IL-2Rβ or ℽ$_c$) while being agitated at 4°C. After approximately 30 minutes, cells were washed again in a chilled buffer and then incubated on ice for 5 minutes with a FITC-conjugated anti-c-Myc antibody (1 uL per 3×10^6 cells) and streptavidin-phycoerythrin (1 uL per 100 uL volume of yeast). Yeast was then washed and counted by flow cytometry (Accuri C6) or sorted by FACS (Sony SH800).

Mutagenesis and affinity maturation:

Site-saturation mutagenesis (SSM) libraries were constructed from synthetic DNA from Genscript. For each amino acid on each design template, forward primers and reverse primers were designed such that PCR amplification would result in a 5' PCR product with a

degenerate NNK codon and a 3' PCR product, respectively. Amplification of "left" and "right" products by COF and COR primers yielded a series of template products each consisting of a degenerate NNK codon at a different residue position. For each design, these products were pooled to yield the SSM library. SSM libraries were transformed by electroporation into conditioned Saccharomyces cerevisiae strain EBY100 cells, along with linearized pETcon3 vector, using the protocol previously described by Benatuil et al. For details of the primers used in the creation of SSM libraries SI Tables S5–6.

Combinatorial libraries were constructed from synthetic DNA from Genscript containing ambiguous nucleotides and similarly transformed into a linearized pETcon3 vector. For details of the primers used in the creation of combinatorial libraries see SI Tables S7–8.

Protein expression:

Genes encoding the designed protein sequences were synthesized and cloned into pET-28b(+) *E. coli* plasmid expression vectors (GenScript, N-terminal 6xHis-tagged followed by a thrombin cleavage site. For all the designed proteins, the sequence of the N-terminal tag used is MGSSHHHHHHSSGLVPRGSHM (unless otherwise noted), which is followed immediately by the sequence of the designed protein. Plasmids were then transformed into chemically competent *E. coli* Lemo21 cells (NEB). Protein expression was performed using Terrific Broth and M salts, cultures were grown at 37°C until OD_{600} reached approximately 0.8, then expression was induced with 1 mM of isopropyl β-D-thiogalactopyranoside (IPTG), and the temperature was lowered to 18°C. After expression for approximately 18 hours, cells were harvested and lysed with a Microfluidics M110P microfluidizer at 18,000 psi, then the soluble fraction was clarified by centrifugation at 24,000 g for 20 minutes. The soluble fraction was purified by Immobilized Metal Affinity Chromatography (Qiagen) followed by FPLC size-exclusion chromatography (Superdex 75 10/300 GL, GE Healthcare). The purified Neo-2/15 was characterized by Mass Spectrum (MS) verification of the molecular weight of the species in solution (Thermo Scientific), Size Exclusion - MultiAngle Laser Light Scattering (SEC-MALLS) in order to verify monomeric state and molecular weight (Agilent, Wyatt), SDS-PAGE, and endotoxin levels (Charles River).

Human and mouse IL-2 complex components including hIL-2 (a.a. 1–133), hIL-2Rα (a.a. 1–217), hIL-2Rβ (a.a. 1–214) hIL-2Rɣ$_c$ (a.a. 1–232), mIL-2 (a.a. 1–149), mIL-2Rα ectodomain (a.a. 1–213), mIL-2Rβ ectodomain (a.a. 1–215), and mɣ$_c$ ectodomain (a.a. 1–233) were secreted and purified using a baculovirus expression system, as previously described[39,43]. For the zippered hIL-2Rβɣ$_c$ heterodimer, the aforementioned extracellular domain residues for the human/mouse IL-2Rβ and human/mouse IL-2Rɣ$_c$ were separately cloned into baculovirus expression constructs containing 3C protease-cleavable basic and acidic leucine zippers, respectively, for a high-fidelity pairing of the receptor subunits, as described previously[52]. The IL-2Rβ and IL-2Rɣ$_c$ constructs were transfected independently and their corresponding viruses were co-titrated to determine optimal infection ratios for equivalent expression of the two chains. Insect cell secretion and purification proceeded as described for IL-2 cytokine and receptor subunits. All proteins were purified to >98% homogeneity with a Superdex 200 sizing column (GE Healthcare) equilibrated in HBS.

Purity was verified by SDS-PAGE analysis. For expression of biotinylated human IL-2 and mouse IL-2 receptor subunits, proteins containing a C-terminal biotin acceptor peptide (BAP)-LNDIFEAQKIEWHE were expressed and purified as described via Ni-NTA affinity chromatography and then biotinylated with the soluble BirA ligase enzyme in 0.5 mM Bicine pH 8.3, 100 mM ATP, 100 mM magnesium acetate, and 500 mM biotin (Sigma). Excess biotin was removed by size exclusion chromatography on a Superdex 200 column equilibrated in HBS.

Neo-2/15 crystal and co-crystal structures:

C-terminally 6xHis-tagged endoglycosidase H (endoH) and murine IL-2Rβ and IL-2Rɣ$_c$ were expressed separately in Hi-five cells using a baculovirus system as previously described. IL-2Rɣ$_c$ was grown in the presence of 5 μM kifunensine. After approximately 72 hours, the secreted proteins were purified from the media by passing over a Ni-NTA agarose column and eluted with 200 mM imidazole in HBS buffer (150 mM NaCl, 10 mM HEPES pH 7.3). EndoH was exchanged into HBS buffer by diafiltration. mIL-2Rɣ$_c$ was deglycosylated by overnight incubation with 1:75 (w/w) endoH. mIL-2Rβ and mIL-2Rɣ$_c$ were further purified and buffer exchanged by FPLC using an S200 column (GE Life Sciences).

Monomeric Neo-2/15 was concentrated to 12 mg/ml and crystallized by vapor diffusion from 2.4 M sodium malonate pH 7.0, and crystals were harvested and flash frozen without further cryoprotection. Crystals diffracted to 2.0 Å resolution at Stanford Synchrotron Radiation Laboratory beamline 12–2 and were indexed and integrated using XDS (Kabsch, 2010). The space group was assigned with Pointless (Evans, 2006), and scaling was performed with Aimless (Evans and Murshudov, 2013) from the CCP4 suite (Winn et al., 2013). Our predicted model was used as a search ensemble to solve the structure by molecular replacement in Phaser (McCoy et al., 2007), with six protomers located in the asymmetric unit. After initial rebuilding with Autobuild (Terwilliger et al., 2008), iterative cycles of manual rebuilding and refinement were performed using Coot (Emsley et al., 2010) and PHENIX (Adams et al., 2010).

To crystallize the ternary Neo-2/15:mIL-2Rβ:mIL-2Rɣ$_c$ complex, the three proteins were combined in equimolar ratios, digested overnight with 1:100 (w/w) carboxypeptidases A and B to remove purification tags, and purified by FPLC using an S200 column; fractions containing all three proteins were pooled and concentrated to 20 mg/ml. Initial needlelike microcrystals were formed by vapor diffusion from 0.1 M imidazole pH 8.0, 1 M sodium citrate and used to prepare a microseed stock for subsequent use in microseed matrix screening (MMS, (D'Arcy et al., 2014)). After a single iteration of MMS, crystals grown in the same precipitant were cryoprotected with 30% ethylene glycol, harvested and diffracted anisotropically to 3.4 Å × 3.8 Å × 4.1 Å resolution at Advanced Photon Source beamline 23ID-B. The structure was solved by molecular replacement in Phaser using the human IL-2Rβ and IL-2Rɣ$_c$ structures (PDB ID: 2B5I) as search ensembles. This produced an electron density map into which two poly-alanine alpha helices could be manually built. Following rigid body refinement in Phenix, electron density for the two unmodeled alpha helices, along with the BC loop and some aromatic side chains, became visible, allowing

docking of the monomeric Neo-2/15. Two further iterations of MMS and use of an additive screen (Hampton Research) produced crystals grown by vapor diffusion using 150 nl of protein, 125 nl of well solution containing 0.1 M Tris pH 7.5, 5% dextran sulfate, 2.1 M ammonium sulfate and 25 nl of microseed stock containing 1.3 M ammonium sulfate, 50 mM Tris pH 7.5, 50 mM imidazole pH 8.0, 300 mM sodium citrate. Crystals cryoprotected with 3 M sodium malonate were flash frozen and diffracted anisotropically to 2.5 Å × 3.7 Å × 3.8 Å at Advanced Light Source beamline 5.0.1. After processing the data with XDS, an elliptical resolution limit was applied using the STARANISO server (Bruhn et al., 2017). Rapid convergence of the model was obtained by refinement against these reflections using TLS and target restraints to the higher resolution human receptor (PDB ID: 2B5I) and Neo-2/15 structures in Buster (Smart et al., 2012; Bricogne et al., 2016), with manual rebuilding in Coot, followed by a final round of refinement in PHENIX with no target restraints. Structure figures were prepared with PyMol (Schrodinger, LLC. 2010. The PyMOL Molecular Graphics System, Version 2.1.0). Software used in this project was installed and configured by SBGrid (Morin et al., 2013).

Cell Lines:

Unmodified YT-1[53] and IL-2Rα[+] YT-1 human NK cells[54] were cultured in RPMI complete medium (RPMI 1640 medium supplemented with 10% fetal bovine serum, 2 mM L-glutamine, minimum non-essential amino acids, sodium pyruvate, 25 mM HEPES, and penicillin-streptomycin [Gibco]). CTLL-2 cells purchased from ATCC were cultured in RPMI complete with 10% T-STIM culture supplement with ConA (Corning). 24 hours prior to signaling studies, CTLL-2 cells were resuspended in RPMI lacking T-STIM culture supplement for IL-2 starvation. Viability (>95%) of CTLL-2 cells was verified by trypan blue exclusion (counted in a hemocytometer) immediately before performing the signaling assays. All cells were maintained at 37°C in a humidified atmosphere with 5% CO_2. The subpopulation of YT-1 cells expressing IL-2Rα was purified via magnetic selection as described previously[39]. Enrichment and persistence of IL-2Rα expression were monitored by analysis of PE-conjugated anti-human IL-2Rα (Biolegend) antibody binding on an Accuri C6 flow cytometer (BD Biosciences).

Circular dichroism (CD):

Far-ultraviolet CD measurements were carried out with an AVIV spectrometer model 420 in PBS buffer (pH 7.4) in a 1 mm path-length cuvette with a protein concentration of ~0.20 mg/ml (unless otherwise mentioned in the text). Temperature melts where from 25 to 95 °C and monitored absorption signal at 222 nm (steps of 2 °C/min, 30 s of equilibration by step). Wavelength scans (195–260 nm) were collected at 25°C and 95°C, and again at 25°C after fast refolding (~5 min).

Binding studies:

Surface plasmon resonance (SPR): For IL-2 receptor affinity titration studies, biotinylated human or mouse IL-2Rα, IL-2Rβ, and IL-2Rɣ$_c$ receptors were immobilized to streptavidin-coated chips for analysis on a Biacore T100 instrument (GE Healthcare). An irrelevant biotinylated protein was immobilized in the reference channel to subtract non-specific binding. Less than 100 response units (RU) of each ligand was immobilized to minimize

mass transfer effects. Three-fold serial dilutions of hIL-2, mIL-2, Super-2, or engineered IL-2 mimetics, were flowed over the immobilized ligands for 60 s and dissociation was measured for 240 s. For IL-2Rβγ_c binding studies, saturating concentrations of hIL-2Rβ (3 uM) or mIL-2Rβ (5 uM) were added to the indicated concentrations of hIL-2 or mIL-2, respectively. Surface regeneration for all interactions was conducted using 15 s exposure to 1 M MgCl2 in 10 mM sodium acetate pH 5.5. SPR experiments were carried out in HBS-P+ buffer (GE Healthcare) supplemented with 0.2% bovine serum albumin (BSA) at 25°C and all binding studies were performed at a flow rate of 50 L/min to prevent analyte rebinding. Data was visualized and processed using the Biacore T100 evaluation software version 2.0 (GE Healthcare). Equilibrium titration curve fitting and equilibrium binding dissociation (KD) value determination was implemented using GraphPad Prism assuming all binding interactions to be first order. SPR experiments were reproduced three times with similar results. Biolayer interferometry: binding data were collected in a Octet RED96 (ForteBio, Menlo Park, CA) and processed using the instrument's integrated software using a 1:1 binding model. Biotinylated target receptors, either human or murine IL-2Rα, IL-2Rβ or γ_c were functionalized to streptavidin-coated biosensors (SA ForteBio) at 1μg/ml in binding buffer (10 mM HEPES [pH 7.4], 150 mM NaCl, 3 mM EDTA, 0.05% surfactant P20, 0.5% non-fat dry milk) for 300 seconds. Analyte proteins were diluted from concentrated stocks into binding buffer. After baseline measurement in binding buffer alone, the binding kinetics were monitored by dipping the biosensors in wells containing the target protein at the indicated concentration (association step) and then dipping the sensors back into baseline/buffer (dissociation). For heterodimeric receptor binding experiments for IL-2Rβγ_c, γ_c was bound to the sensor while IL-2Rβ was in solution at saturating concentrations(i.e. at least ~2.5 fold molar excess over the K_d).

STAT5 phosphorylation studies:

In vitro studies: Approximately 2×10^5 YT-1, IL-2Rα$^+$ YT-1, or starved CTLL-2 cells were plated in each well of a 96-well plate and re-suspended in RPMI complete medium containing serial dilutions of hIL-2, mIL-2, Super-2, or engineered IL-2 mimetics. Cells were stimulated for 15 min at 37°C and immediately fixed by addition of formaldehyde to 1.5% and 10 min incubation at room temperature. Permeabilization of cells was achieved by resuspension in ice-cold 100% methanol for 30 min at 4°C. Fixed and permeabilized cells were washed twice with FACS buffer (phosphate-buffered saline [PBS] pH 7.2 containing 0.1% bovine serum albumin) and incubated with Alexa Fluor® 647-conjugated anti-STAT5 pY694 (BD Biosciences) diluted 1:50 in FACS buffer for 2 hr at room temperature. Cells were then washed twice in FACS buffer and MFI was determined on a CytoFLEX flow cytometer (Beckman-Coulter). Dose-response curves were fitted to a logistic model and half-maximal effective concentration (EC_{50} values) and corresponding 95% confidence intervals were calculated using GraphPad Prism data analysis software after subtraction of the mean fluorescence intensity (MFI) of unstimulated cells and normalization to the maximum signal intensity. Experiments were conducted in triplicate and performed three times with similar results. *Ex vivo* studies: Spleens and lymph nodes were harvested from wild-type C57BL/6J or B6;129S4-Il2ra^{tm1Dw} (CD25KO) mice purchased from The Jackson Laboratory and made into a single cell suspension in sort buffer (2% Fetal Calf Serum in pH 7.2 phosphate-buffered saline). CD4+ T cells were enriched through negative selection by

staining the cell suspension with biotin-conjugated anti-B220, CD8, NK1.1, CD11b, CD11c, Ter119, and CD19 antibodies at 1:100 for 30 min on ice. Following a wash with sort buffer, anti-biotin MicroBeads (Miltenyi Biotec) were added to the cell suspension at 20 μL per 10^7 total cells and incubated on ice for 20 minutes. Cells were washed and then resuspended. Negative selection was then performed using EasySep Magnets (STEMCELL Technologies). Approximately 1×10^5 enriched cells were added to each well of a 96-well plate in RPMI complete medium with 5% FCS with 10-fold serial dilutions of mIL-2, Super-2, or Neo-2/15. Cells were stimulated for 20 min at 37°C in 5% CO_2, fixed with 4% PFA and incubated for 30 minutes at 4°C. Following fixation, cells were harvested and washed twice with sort buffer and again fixed in 500 μL 90% ice-cold methanol in dH_2O for 30 min on ice for permeabilization. Cells were washed twice with Perm/Wash Buffer (BD Biosciences) and stained with anti-CD4-PerCP in Perm/Wash buffer (1:300), anti-CD44-Alexa Fluor 700 (1:200), anti-CD25-PE-Cy7 (1:200), and 5 μL per sample of anti-pSTAT5-PE pY694 for 45 min at room temperature in the dark. Cells were washed with Perm/Wash and re-suspended in sort buffer for analysis on a BD LSR II flow cytometer (BD Biosciences). Dose-response curves were fitted to a logistic model and EC50 values and corresponding 95% confidence intervals were determined using GraphPad Prism data analysis software after subtraction of the MFI of untreated cells and normalization to the maximum signal intensity. Experiments were performed in triplicate and repeated three times with similar results.

In vivo murine airway inflammation experiments:

Mice (C57BL/6J, purchased from The Jackson Laboratory) were inoculated intranasally with 20μL of whole house dust mite antigen (Greer) resuspended in PBS to a total of 23μg Derp1 per mouse. From Days 1–7, mice were given a daily intraperitoneal injection of 20μg mIL-2 in sterile PBS (pH 7.2), a molar equivalent of Neo-2/15 in sterile PBS, or no injection. On Day 8, circulating T cells were intravascularly labeled and tetramer-positive cells were enriched from lymph nodes and spleen or lung as previously described (Hondowicz, Immunity, 2016). Both the column flow-through and bound fractions were saved for flow cytometry analysis. Cells were surface stained with antibodies and analyzed on a BD LSR II flow cytometer with BD FACSDiva software (BD Biosciences). Antibodies used: FITC anti-Ki67, clone SolA15, PerCP-Cy5.5 anti-CD25, clone PC61, eFluor 450 anti-Foxp3, clone FJK-16S, BV510 anti-CD8, clone 53–6.7, BV605 anti-PD-1, clone J43, BV711 anti-CD4, clone RM4–5, BV786 anti-CD62L, clone MEL-14, PE anti-CD69, clone H1.2F3, PE-CF594 anti-B220, clone RA3–6B2, PE-Cy7 anti-CXCR5, clone 2G8 and BUV395 anti-Thy1.2, clone 53–2.1. All flow cytometry files were analyzed using FlowJo 9.9.4 and statistical analysis was performed using Prism 7. All experiments were performed in accordance with the University of Washington Institutional Care and Use Committee guidelines.

Colorectal carcinoma *in vivo* mice experiments:

CT26 cells were sourced from Jocelyne Demengeot's research group at IGC (Instituto Gulbenkian de Ciência), Portugal. On day 0, 5×10^5 cells were injected subcutaneously (s.c.) into the flanks of BALB/c mice purchased from Charles River with 50 μL of a 1:1 mixture of Dulbecco's modified Eagle medium (Gibco) with Matrigel (Corning). Starting on

day 6, when tumor volume reached around 100mm3, Neo-2/15 and mIL-2 (Peprotech) were administered daily by intraperitoneal (i.p.) injection in 50 μL of PBS (Gibco). Mice were sacrificed when tumor volume reached 1,300 mm3. BALB/c mice were purchased from Charles River. <u>Flow cytometry</u>: All reagents were purchased from Gibco by Life Technologies (Thermo Fisher Scientific) unless stated otherwise. Excised tumors were minced and digested using a mix of collagenase I, collagenase IV (Worthington) and DNase I (Roche) in a shaker for 20 minutes, 250 rpm at 37°C. After digestion, samples were passed through a 100μm cell strainer, and resuspended in cold complete RPMI 1640 medium, supplemented with 10 mM of HEPES buffer, 1 mM of sodium pyruvate, 50μM of 2-mercaptoethanol, 100 U/mL of penicillin and 100 μg/mL of streptomycin and complemented with 1% non-essential amino acids (NEAA), 1% GlutaMAX supplement and 10% heat-inactivated fetal bovine serum (HI FBS). The cell suspensions from the spleens and the inguinal lymph nodes were obtained through the smashing of the tissues against the filter of a 100μm cell strainer. Cells were resuspended in PBS with 2% FBS and 1mM EDTA and stained for extracellular markers for 45 min at 4°C. Cell suspensions were then fixed, permeabilized and stained for intracellular markers using the eBioscience™ Foxp3 / Transcription Factor Staining Buffer Set from ThermoFisher Scientific. Samples were analyzed in a BD LSRFortessa™ flow cytometer equipped with a BD FACSDiva software™ and data were analyzed in FlowJo V10 software and the statistical analysis performed using Prism 5. Antibodies (BioLegend) used in colon carcinoma experiments were: CD45-BV510 (30-F11), CD3-BV711 (17A2), CD49b-FITC (DX5), CD4-BV605 (RM4–5), CD8-PECy7 (53–6.7), and Foxp3-APC (FJK-16s; eBioscience). Fixable Viability Dye eFluor 780 (eBioscience) was used to exclude dead cells. Animals were maintained according to protocols approved by the Direção Geral de Veterinária and iMM Lisboa ethical committee.

Melanoma in vivo experiments:

B16F10 cells were purchased from ATCC. On day 0, 5×10^5 cells were inoculated into the mice (C57BL/6J purchased from Jackson) by s.c. injection in 500 μL of Hank's Balanced Salt Solution (Gibco). Starting on the specified day, Neo-2/15 or mIL-2 (Peprotech) treatments were administered daily by intraperitoneal (i.p.) injection in 200 μL of LPS-free PBS (Teknova). Treatment with TA99 (a gift from Noor Momin and Dane Wittrup, Massachusetts Institute of Technology) at 150 μg/mouse was added later at the (as indicated). Mice were sacrificed when tumor volume reached 2,000 mm3. <u>Flow cytometry</u>: Excised tumors were minced, enzymatically digested (Miltenyi Biotec), and passed through a 40-μm filter. Cells from spleens and tumor-draining lymph nodes were dispersed into PBS through a 40-μm cell strainer using the back of a 1-mL syringe plunger. All cell suspensions were washed once with PBS, and the cell pellet was resuspended in 2% inactivated fetal calf serum containing fluorophore-conjugated antibodies. Cells were incubated for 15 minutes at 4°C then fixed, permeabilized, and stained using a BioLegend FoxP3 staining kit. Samples were analyzed on a BD Fortessa flow cytometer. Antibodies (BioLegend) used in melanoma experiments were: CD45-BV711 (clone 30-F11), CD8-BV650 (53–6.7), CD4-BV421 (GK1.5), TCRβ-BV510 (H57–597), CD25-AF488 (PC61), FoxP3-PE (MF-14). Animals were maintained according to protocols approved by Dana–Farber Cancer Institute (DFCI) Institutional Animal Care and Use Committee.

Generation of anti-Neo-2/15 polyclonal antibody:

Mice (C57BL/6J purchased from Jackson) were injected i.p . with 500 μg of K.O. Neo-2/15 in 200 μL of a 1:1 emulsion of PBS and Complete Freund's Adjuvant. Mice were boosted on days 7 and 15 with 500 μg of K.O. Neo-2/15 in 200 μL of a 1:1 emulsion of PBS and Incomplete Freund's Adjuvant. On day 20, serum was collected and recognition of Neo-2/15 was confirmed by ELISA. For the ELISA, plates were coated with Neo-2/15, K.O. Neo-2/15, or mIL-2 mixed with ovalbumin for a total of 100 ng/well in carbonate buffer. Coated plates were incubated with murine serum diluted 1:1000 in PBS. Binding was detected using anti-mouse IgG conjugated to HRP and developed with TMB. Results were quantified using absorption at 450 nm.

Enzyme-linked immunosorbent assay (ELISA):

High-binding 96-well plates (Corning) were coated overnight at 4°C with 100 ng/mL of Neo-2/15, mIL-2 (Peprotech), hIL-2 (Peprotech), or ovalbumin (Sigma-Aldrich) in carbonate buffer. Antibody binding to target proteins was detected using HRP-conjugated sheep anti-mouse IgG (GE Healthcare) at 75 ng/mL. Plates were developed with tetramethylbenzidine and HCl. Absorbance was measured at 450 nm with an EnVision Multimode Plate Reader (PerkinElmer).

T cell proliferation assay:

Cells were isolated from mice (C57BL/6J purchased from Jackson) spleens using the EasySep T Cell Isolation Kit (Stemcell Technologies). Cells were plated in RPMI in 96-well culture plates at a density of 10,000 cells/well. Media were supplemented with regular or heat-treated Neo-2/15, rmIL-2, or Super-2 (as indicated). After 5 days of incubation at 37°C, cell survival and proliferation were measured by CellTiter-Glo Luminescent Cell Viability Assay (Promega).

In vivo experiments:

For Treg expansion experiments (Figure 4a), naive C57BL/6 mice were treated daily with Neo-2/15 or mIL-2 at the indicated concentrations (n=2–3 per group). After 14 days, spleens were harvested and analyzed by flow cytometry using the indicated markers; For immunogenicity experiments (Figure 4c), C57BL/6 mice were inoculated with 5×10^5 B16F10 cells by subcutaneous injection. Starting on day 1, mice were treated daily with Neo-2/15 (10 μg) or equimolar mIL-2 by intraperitoneal (i.p.) injection (n=10 for each group). After 14 days, serum (antiserum) was collected and IgG was detected by ELISA in plates coated with fetal bovine serum (FBS 10%, negative control), Neo-2/15, mIL-2, hIL-2, or Ovalbumin (OVA) as a negative control. Polyclonal mouse IgG against Neo-2/15 (Anti-Neo-2/15 pAb) was generated using complete Freund's adjuvant in conjunction with a knockout of Neo-2/15 ("K.O. Neo-2/15", which is an inactive double point mutant of Neo-2/15: Y14D, F99D); For Colorectal cancer experiments (Figure 4d), BALB/C mice were inoculated with CT26 tumors. Starting on day 6, mice were treated daily with i.p. injection of mIL-2 or Neo-2/15 (10 μg), or left untreated (n = 5 per group); For Melanoma experiments (Figure 4e), C57BL/6 mice were inoculated with B16 tumors as in "a)". Starting on day 1, mice were treated daily with i.p. injection of Neo-2/15 (10 μg) or

equimolar mIL-2 (n = 10 per group). Twice-weekly treatment with TA99 was added on day 3. Mice were euthanized when weight loss exceeded 10% of initial weight or when tumor size reached 2,000 mm3; For CD8$^+$: Treg ratio in Melanoma experiments (Figure 4f), C57BL/6 mice were inoculated with B16 tumors and treated by daily i.p. injection as indicated. Treatment with TA99 (bottom plot) was started on day 5 and continued twice-weekly. Tumors were harvested from mice when they reached 2,000 mm3 and analyzed by flow cytometry. The CD8$^+$: Treg cell ratio was calculated by dividing the percentage CD45+ TCRβ+ cells that were CD8+ by the percentage that were CD4+ CD25+ FoxP3+.

CAR-T cell in vivo experiments:

In vitro T cell proliferation assay. Primary human T cells were obtained from healthy donors, who provided written informed consent for research protocols approved by the Institutional Review Board of the FHCRC. Peripheral blood mononuclear cells (PBMC) were isolated by centrifugation over Ficoll-Hypaque (Sigma). T cells were isolated using EasySep™ CD8 or CD4 negative isolation kits (STEMCELL Technologies). To stimulate T cells, T cells were thawed and incubated with anti-CD3/CD28 Dynabeads (Gibco) at 1:1 ratio in media supplemented with 50 IU/ml (3.1ng/ml) of IL2. Beads were removed after four days of incubation. Stimulated or freshly thawed unstimulated T cells were plated at 30000 or 50000 cells/well, respectively, in 96 well format and cultured in indicated concentrations of IL-2 or Neo-2/15 in triplicate. Three days later, proliferation was measured using CellTiter-Glo 2.0. (Promega). In vivo RAJI experiment: The FHCRC Institutional Animal Care and Use Committee approved all mouse experiments. Six- to eight-week-old NSG mice were obtained from the Jackson Laboratory. 0.5*10^6 RAJI tumor cells transduced with (ffLuc)-eGFP were tail vein injected into the NSG mice. Seven days post tumor inject, lentiviral transduced anti-CD19 CAR T cells (0.4*10^6 CD4, 0.4*10^6 CD8) prepared as described in (Liu et al, 2016) were infused i.v. into mice. hIL2 or Neo-2/15 at 20μg/mouse were given i.p. from day 8 to 16 post tumor injection.

Disulfide-stapling Neo-2/15 to increase its stability and binding potency.—
Neo-2/15 is highly modular, allowing to further tune its properties. As proof of concept, we designed stability enhancing disulfide staples that preserve the protein's function intact[55]. Two computational design strategies were tested, first, we designed internal disulfide bridges for all pairs of positions with favorable geometrical arrangements inside of Neo-2/15. The four best disulfide-stapled designs (i.e. with the most favorable energy and minimal geometric distortion) were recombinantly expressed (*E. coli*). A design that bridges residues 38–75 (stabilizing helices H3->H2') was confirmed to be monomeric (SEC-MALS). In the second approach, we remodeled the N- C-terminus of Neo-2/15 to allow the introduction of a single-disulfide staple encompassing the entire protein. We generated a total of 330 models that were then filtered based on fragment quality and disulfide bond geometry. Finally, the designs were manually inspected and six were selected (representing a diversity of insertion lengths) and experimentally characterized as described above. One design, replacing the terminal residues P- and -S with the amino acid sequences CNSN- and -NFQC (N- and C-termini, respectively) (extended Fig. E3) was confirmed to be monomeric (SEC-MALS). The designs from both disulfide stapling strategies successfully increased the stability of Neo-2/15 (Tm > 95°C) and its binding potency (extended Fig. E3).

Pharmacodynamics and pharmacokinetics of Neo-2/15 in mice.—We assessed the *in vivo* duration of pSTAT5 signaling response to Neo-2/15 in peripheral blood lymphocytes of naive mice (CD8 and B cells, see extended Fig. E6). As expected, Neoleukin-2/15 has a significant effect (similar to mIL-2) in CD8 cell signaling one-hour after administration, but as expected from Neo-2/15 small size, the signaling effect decreases greatly after 3-hours (see extended Fig. E6) and is undetectable after 8-hours (data not shown). This suggests that future engineering of Neo-2/15 to extend half-life --there are a number of approaches such as Fc-fusions, site-specific PEGylation (e.g. through engineered cysteines, such as those demonstrated in SI Figure S14), fusions to targeting domains (e.g. mAbs, sdAbs or VHHs[12,56], DARPins[56], or de novo designed binding proteins[35,57,58]) can be used to extend its half-life and would likely translate into improved pharmacokinetics.

Molecular dynamics (MD) simulations of apo-Neo-2/15 and holo-Neo-2/15.—Molecular dynamics (MD) simulations in explicit water solvent initiated from the computational model of apo-Neo-2/15 recapitulated the crystallographic structure of (monomeric) apo-Neo-2/15 (avg r.m.s.d$_{C\alpha}$ to crystal structure = 1.9 Å, see extended Fig. E7a). For instance, MD simulations initiated from the ternary complex of Neo-2/15 with the mIL-2Rβγ$_c$ were more likely to sample the crystallographic structure observed for Neo-2/15 in the ternary complex with mIL-2Rβγ$_c$, including the outward movement of helices H2'-H4 (Neo-2\15 avg r.m.s.d$_{C\alpha}$ to crystal structure = 1.4 Å, see extended Fig. E7c). The conformation of Neo2/15 seems to be stabilized in the ternary complexes (either with the murine or human receptors, see extended Fig. E7c–d). Molecular Dynamics simulations were performed using GROMACS 2018.1[59,60] with the Amber99SB-ILDN force field[61]. Each system consisted of the protein in a solvated dodecahedron box (min initial distance from the protein to the boundary = 1 nm) filled with explicit TIP3P waters[62] and neutralized with Cl⁻ or Na⁺ ions. The solvated systems were energy-minimized using the steepest descent minimization method, followed by equilibration for 200 ps under the NPT ensemble with position restraints (1000 kJ mol⁻¹ nm⁻¹, applied on all the proteins' heavy atoms). Pressure coupling to 1 atm was performed with the Berendsen barostat[63], and the temperature was coupled to 310 K using the velocity-rescaling thermostat. The equilibrated systems were used as starting conformations for production runs. In the case of the monomers, we performed 5 independent production simulations of 100 ns/each, and for the complexes bound to any of the IL-2 receptors, we performed 5 independent simulations of 90 ns/each. The production simulations were conducted under the NPT ensemble, with the Parrinello-Rahman barostat[64] for pressure coupling to 1 atm. The cutoff for van der Waals and short-range electrostatic interactions was set to 1 nm. Long-range electrostatic interactions were treated with the Particle-Mesh Ewald (PME) summation method[65], and the Verlet cut-off scheme was used[66]. The LINCS algorithm was used to constrain all chemical bonds and allow an integration time-step of 2 fs. The simulation trajectories were recorded every 20 ps and were analyzed using GROMACS.

Statistical and power analyses:

For statistical test a P-value of less than 0.05 considered significant, unless otherwise noted. For comparison of fitted curves in cellular phospho-STAT5 signaling assays, differences in EC$_{50}$ values were considered statistically significant if their 95% confidence intervals did

not overlap. In vivo airway inflammation experiments: comparison of cell populations were performed using a two-tailed t-test. In vivo murine Colon cancer experiments: comparisons of the survival of tumor-bearing mice were performed using the log-rank Mantel-cox test (95% confidence interval). Comparisons of weight loss in tumor-bearing mice were performed using a two-tailed t-test. In vivo murine Melanoma experiments: comparisons of the survival of tumor-bearing mice were performed using the log-rank Mantel-cox test (95% confidence interval). Comparisons of weight loss in tumor-bearing mice were performed using a two-tailed t-test. The minimum group size was determined using G*Power for an expected large effect size (Cohen's d = 1.75). For all the bar-plots, the whiskers represent ∓1-standard deviation and individual data points are shown (as dots) for experiments where the n<5. Unless otherwise noted, results were analyzed by one-way ANOVA, if significant (95% confidence interval), post-hoc t-tests were performed comparing groups, and P-values adjusted for multiple comparisons are reported.

Software:

The design of *de novo* protein mimics was performed using custom code (i.e. "Protein Mimic Designer") programmed in Python[67], IPython[68], and using the scientific high-performance modules: PyRosetta[42], numpy and scipy[69,70], matplotlib[71], sklearn[72], cython[73] and pandas[74]. Data analyses were performed with custom code in Python and IPhyton. Protein sequence design was performed with Rosetta[40,41] and RosettaScripts[40]. Protein visualization was performed using PyMOL[75]. Simple protein-protein sequence alignments were performed using BLASTP, and structural based sequence comparisons were performed using MICAN[76]. Sequence logos were generated with WebLogo[77].

Data availability:

PDB structures for Neo-2/15 monomer and its ternary complex with mIL-2R$\beta\gamma_c$ are available in the RCSB Protein Data Bank (PDB IDs: 6DG6 and 6DG5, respectively), diffraction images have been deposited in the SBGrid Data Bank (IDs: 587 and 588, respectively) and validation reports are part of the supplementary information. The *de novo* "Protein Mimic Designer" algorithm and databases used for designing the protein mimetics are available in the online repository Zenodo (doi: "to be provided with the final manuscript"). Other data and materials are available upon request to the corresponding authors.

Extended Data
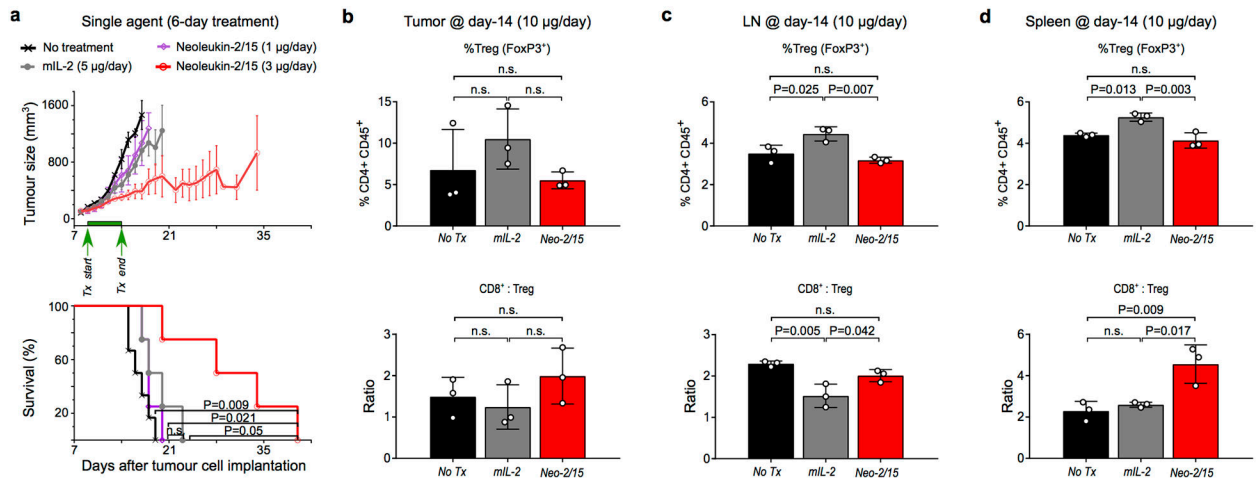
Figure E1. Therapeutic effect of Neo-2/15 on colon cancer.

a) BALB/C mice were inoculated with CT26 tumors. Starting on day 9 and ending on day 14, mice were treated daily with i.p. injection of mIL-2 or Neo-2/15 at the specified concentrations (n = 4 per group), or were left untreated (n=6 per group). Tumor growth curves (top) show data only for surviving mice and stop if a mice/group fell below 50% of the initial number of subjects. Survival curves (*bottom*). Mice were euthanized when weight loss exceeded 10% of initial weight or when tumor size reached 1,300 mm^3. The experiments were performed twice with similar results. **b-d)** The bar-plots compare the T cell populations for BALB/C mice (n=3 per group) that were inoculated with CT26 tumors and treated starting from day 6 with by daily i.p. injection of 10μg of Neo-2/15 or 10μg mIL-2 or no-treatment (No Tx). On day 14 the percentage of Treg cells (CD4$^+$ CD45$^+$ FoxP3$^+$, top graph) and CD8:Treg cell ratio ((CD45$^+$ CD3$^+$ CD8$^+$)/ Treg, bottom graph) was assessed in: b) tumors, c) neighboring inguinal lymph node (LN), and d) spleen. Whiskers represent ∓1-standard deviation and are centered in the mean. Results were analyzed by one-way ANOVA (95% confidence interval), except for survival curves that were assessed using the Mantel-cox test (95% confidence interval). The experiments performed twice with similar results. In all cases, whiskers are centered on the mean and in bar plots represent ∓1-standard deviation, while in growth curves represent ∓1-standard error of the mean. Results were analyzed by one-way ANOVA (95% confidence interval), except for survival curves that were assessed using the Mantel-cox test (95% confidence interval).
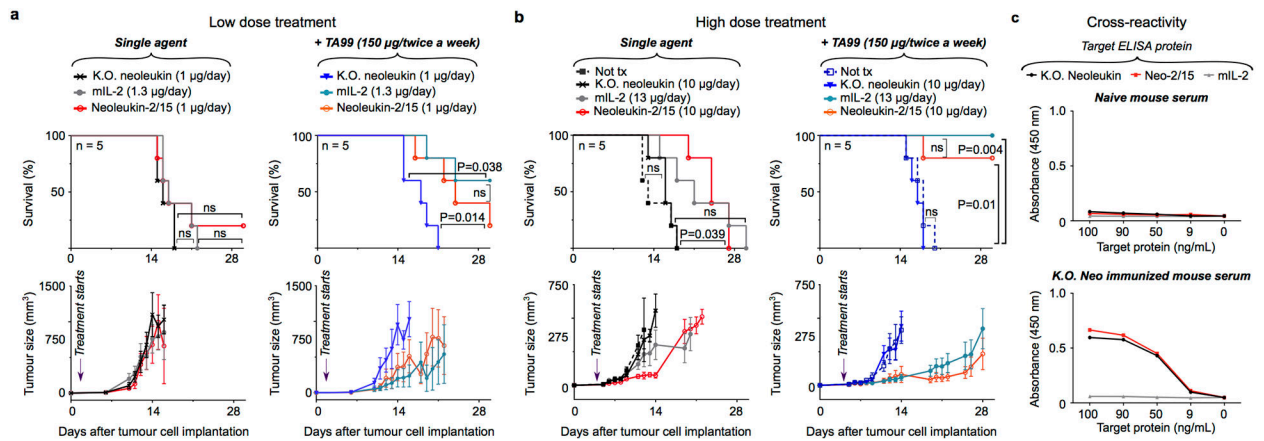
Figure E2. Therapeutic effect of Neo-2/15 on melanoma.

Survival curves (*top*) and tumor growth curves (*bottom*) for C57BL/6 mice that were inoculated with B16 tumors (as in Fig. 4a) and treated with low (1 μg/mice/day) or high doses of Neo-2/15 (10 μg/mice/day). **a)** Starting on day 1, mice (n = 5 per group) were treated daily with i.p. injection of <u>left</u>: single agent Neo-2/15 at 1 μg/mice or equimolar mIL-2, or <u>right</u>: the same treatments in combination a twice-weekly treatment with TA99 (started on day 5). Mice were euthanized when tumor size reached 2,000 mm^3. Tumor growth curves show data only for surviving mice and stop if a mice/group fell below 50% of the initial number of subjects. The experiments were performed twice with similar results; **b)** similar to "a", but starting on day 4, mice (n = 5 per group) were treated daily with i.p. injection of <u>left</u>: single agent Neo-2/15 at 10 μg/mice or equimolar mIL-2; <u>right</u>: the same treatments in combination a twice-weekly treatment with TA99 (started on day 4). Mice were euthanized when tumor size reached 1,000 mm^3. The therapeutic effect of Neo-2/15 is dose-dependent (higher doses are better) and is potentiated in the presence of the antibody TA99. Tumor growth curves show data only for surviving mice and stop if a mice/group fell below 50% of the initial number of subjects. The experiments were performed twice with similar results; **c)** C57BL/6 mice were immunized with 500 μg K.O. Neo-2/15 in complete Freund's adjuvant and boosted on days 7 and 15 with 500 μg K.O. Neo-2/15 in incomplete Freund's adjuvant. Reactivity against K.O. Neo-2/15 and native Neo-2/15 and cross-reactivity with mIL-2 were determined by incubation of serum (diluted 1:1000 in PBS) with plate-bound K.O. Neo-2/15, Neo-2/15, or mIL-2 as indicated. Serum binding was detected using an anti-mouse secondary antibody conjugated to HRP followed by incubation with TMB. Data are reported as optical density at 450 nm. <u>Top</u>: naive mouse serum; <u>bottom</u>: immunized serum. The experiments were performed once. In all the growth curves the whiskers represent ∓1-standard error of the mean. Results were analyzed by one-way ANOVA (95% confidence interval), except for survival curves that were assessed using the Mantel-cox test (95% confidence interval).
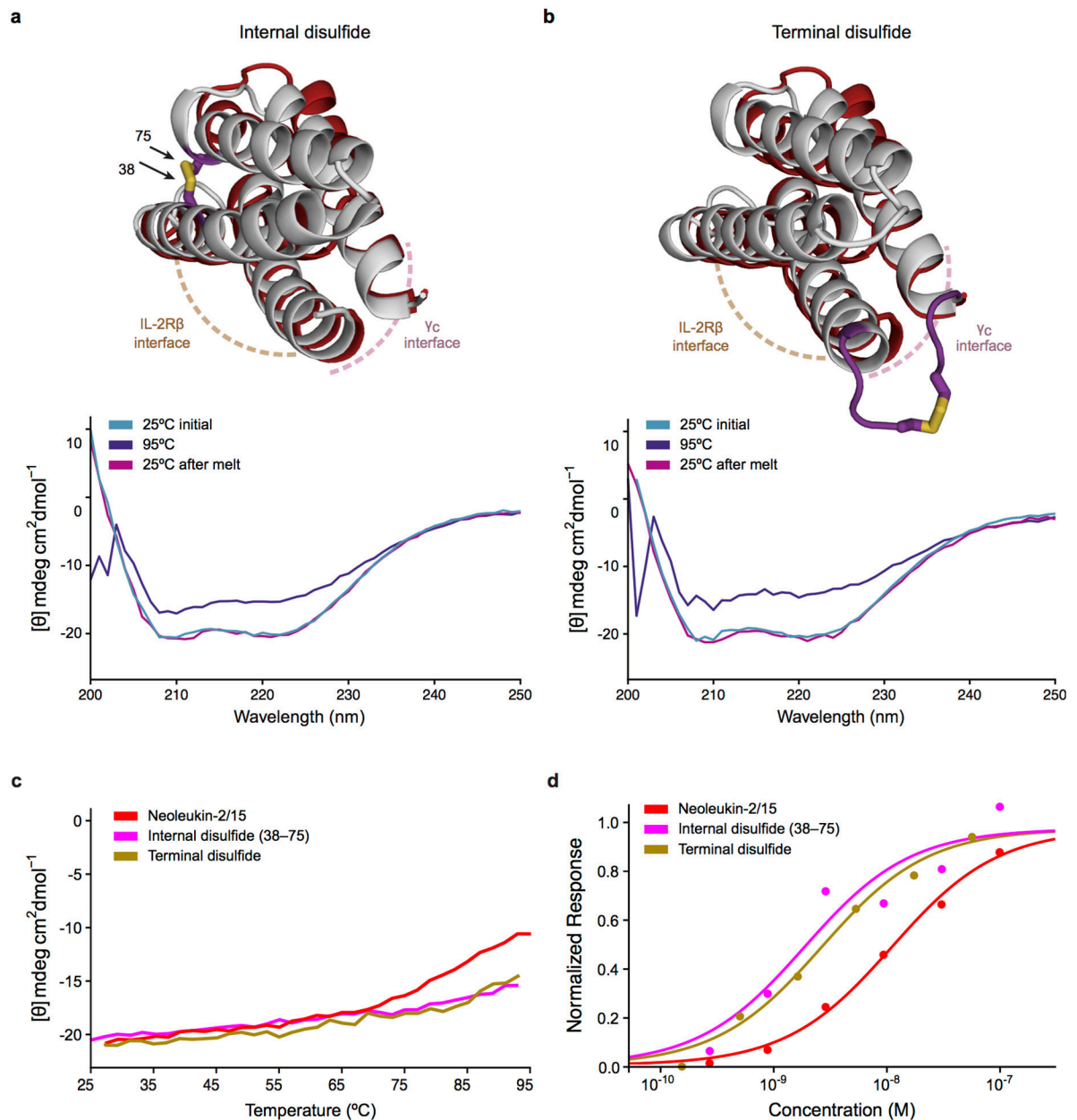
Figure E3. Single disulfide-stapled variants of Neo-2/15 with higher thermal stability.
Structural models of disulfide-stabilized variants of Neo-2/15 (gray) are shown superposed on the ternary crystal structure of Neo-2/15 (red) with mutated residues highlighted in magenta and the disulfide bond shown in gold. Two strategies were used to generate the disulfide stapled variants: **a) (top)** internal placement of the disulfide linking residues 38 and 75. The plot at the **(bottom)** is the experimental CD spectra of the design at 25°C, 95°C and then cooled back to 25°C, complete ellipticity-spectra recovery (full reversibility) upon cooling was observed; **b) (top)** for the terminal disulfide variant, three residues were added to each terminus in order to allow the disulfide to be formed without generating distortions to Neo-2/15's structure. The plot at the **(bottom)** is the experimental CD spectra of the design at 25°C, 95°C and then cooled back to 25°C, complete ellipticity-spectra recovery

(full reversibility) upon cooling was observed; **c)** thermal melts of each disulfide variant in panel "a) and b)" were followed by its circular dichroism signal (222 nm) from 25°C to 95°C (heating rate ~2°C/min). Each of the disulfide-stapled variants shows improved stability relative native Neo-2/15; **d)** the binding strength of each disulfide variant was measured by biolayer interferometry, showing that the introduction of the disulfide bonds does not disrupt binding. Furthermore, both disulfide variants exhibit an improvement in binding IL-2R$\beta\gamma_c$ (Kd ~ 1.3 ± 0.49 and 1.8 ± 0.26 nM, for the internal and external disulfide-staples, respectively), compared to Neo-2/15 (Kd ~ 6.9 ± 0.61 nM for) under the same experimental conditions. These results are consistent with the expected effect of disulfide-induced stabilization on a de novo protein binding site[55]. Thermal denaturation experiments performed 3 times with similar results, and binding experiments were performed once.
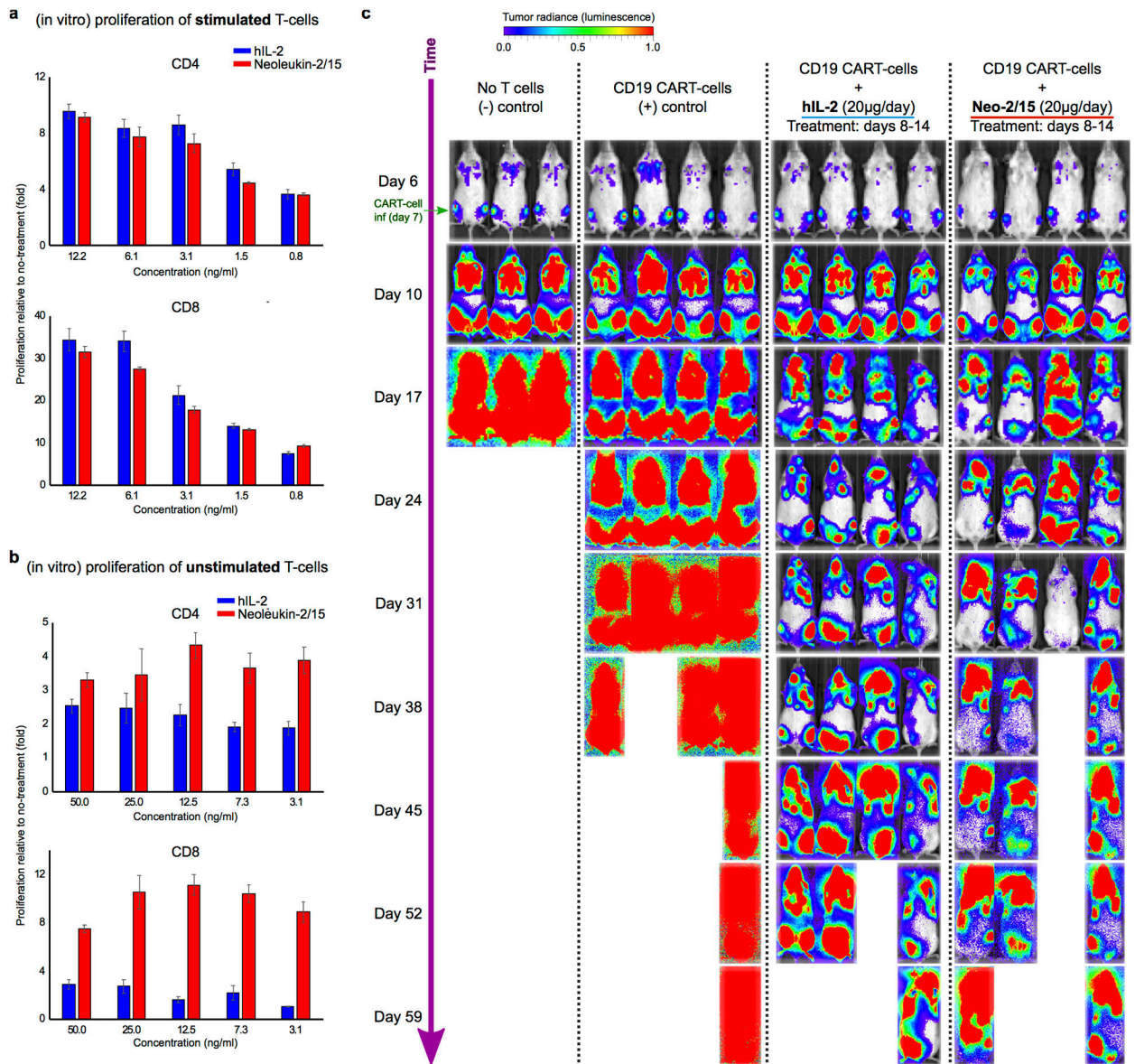
Figure E4. The stimulatory effect of Neo-2/15 on human CAR-T cells.
a) Anti-CD3/CD28 stimulated or **b)** unstimulated human primary CD4 (top) or CD8 (bottom) T cells were cultured in indicated concentrations of human IL-2 or Neo-2/15. T cell proliferation is measured as fold change over T cells cultured without IL-2 supplement. The experiments were performed 3 times with similar results. Whiskers represent ∓1-standard deviation and are centered in the mean; **c)** NSG mice inoculated with 0.5×10^6 RAJI tumor cells were treated with 0.8×10^6 anti-CD19 CAR-T cells 7 days post tumor inoculation. Tumor growth was analyzed by bioluminescence imaging. The experiment was performed once.
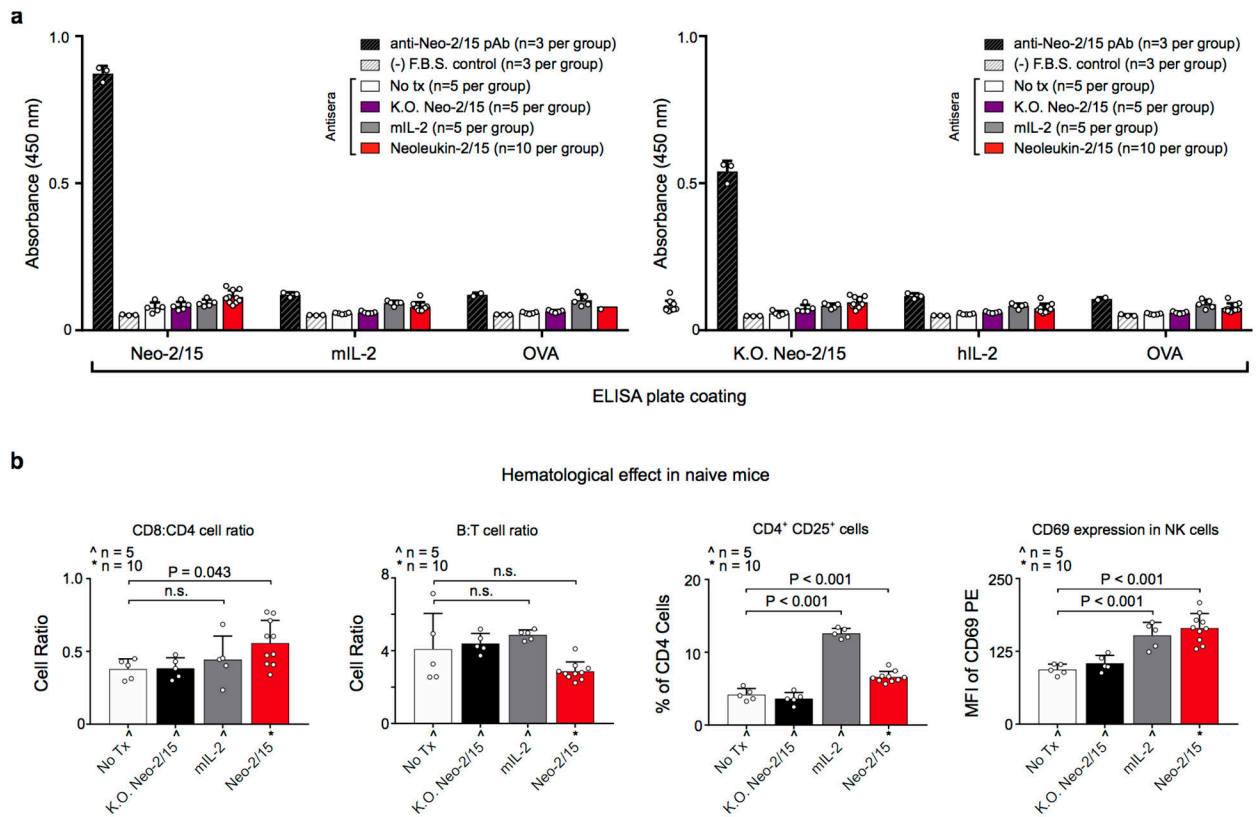
Figure E5. Immunogenicity of Neo-2/15 in healthy naive mice.

**a)** Naive C57BL/6 mice were treated daily with Neo-2/15 (n = 10), K.O. Neo-2/15 (n = 5), mIL-2 (n = 5) or left untreated (n = 5). After 28 days, blood was drawn and analyzed. IgG against Neo-2/15, mIL-2, hIL-2, K.O. Neo-2/15, and ovalbumin were detected in treated-mouse sera diluted 1:100 by ELISA. 10% fetal bovine serum was used as a negative control. Polyclonal antibody against Neo-2/15 was used as a positive control. All statistical comparisons between sera from treated mice and negative control serum were not significant (two-way ANOVA with a 95% confidence interval). All statistical comparisons between Neo-2/15 and mIL-2 treated mice serum were not significant (two-way ANOVA with a 95% confidence interval). The experiments were performed once. **b)** After 14 days, immune cell populations in the blood of treated mice were quantified by flow cytometry. B : T cell ratio (top right) was calculated by dividing the percentage of B220+ cells by the percentage of CD3+ cells. CD8+ : CD4+ cell ratio (top left) was calculated by dividing the percentage of CD3+ cells that were CD8+ by those that were CD4+. NK cells (bottom left) were identified by their expression of NK1.1. Results were analyzed by one-way ANOVA (95% confidence interval). The experiments were performed once. In all cases, whiskers represent ∓1-standard deviation and are centered in the mean.
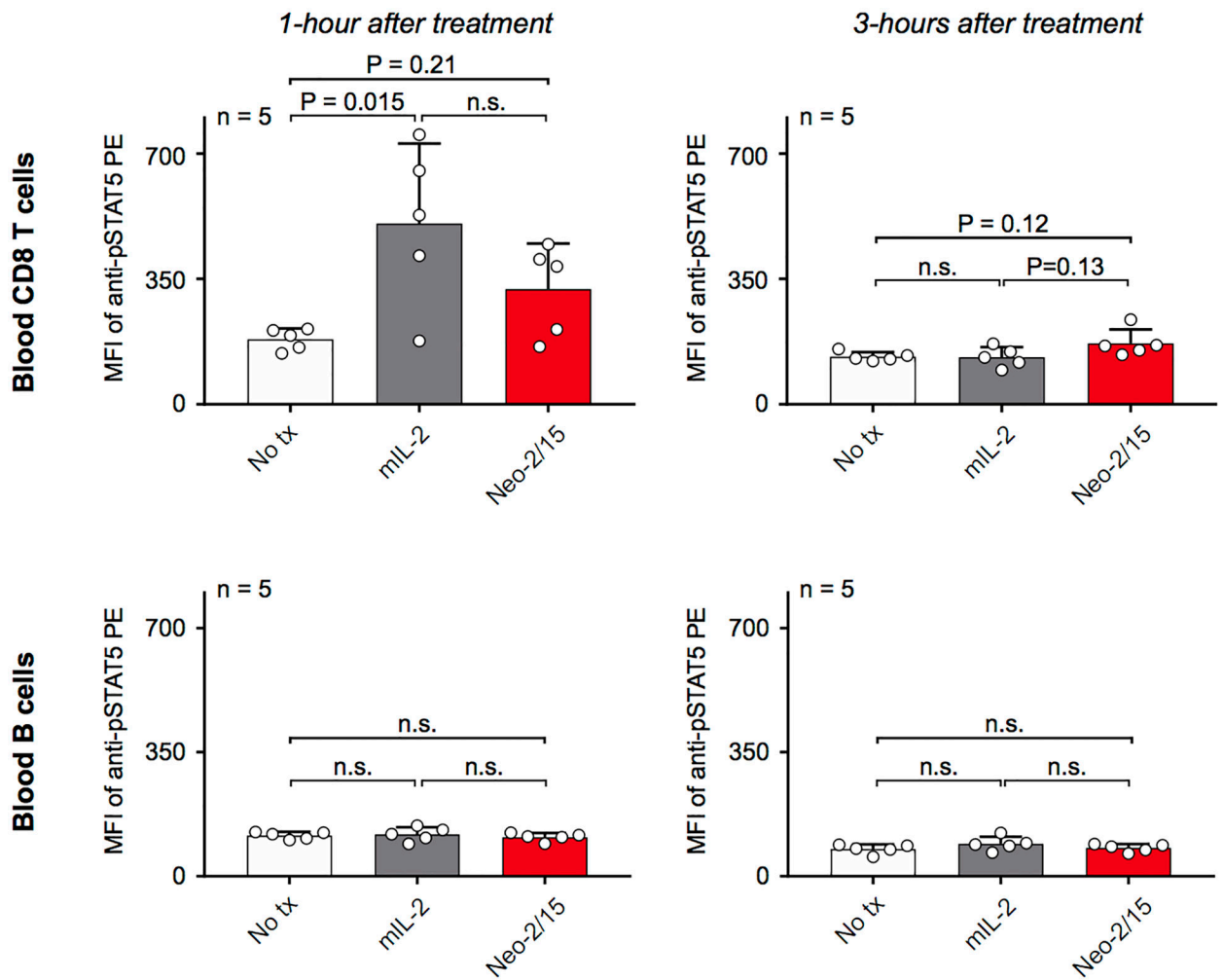
Figure E6. Kinetics of phosphorylation of STAT5 with Neo-2/15 treatment.
Naive C57BL/6 mice were treated once with 13 μg mIL-2 (n = 5) or 10 μg Neo-2/15 (n = 5), or were left untreated (n = 5). Phosphorylation of STAT5 was measured in peripheral blood at the indicated time points by flow cytometry using an anti-pSTAT5 antibody (eBioscience). Mean fluorescence intensity (MFI) is reported at each time point for TCRβ+ CD8+ cells (top) and TCRβ- B220+ cells (bottom). Whiskers represent ∓1-standard deviation and are centered in the mean. Results were analyzed by one-way ANOVA (75% confidence interval). The experiments were performed once.
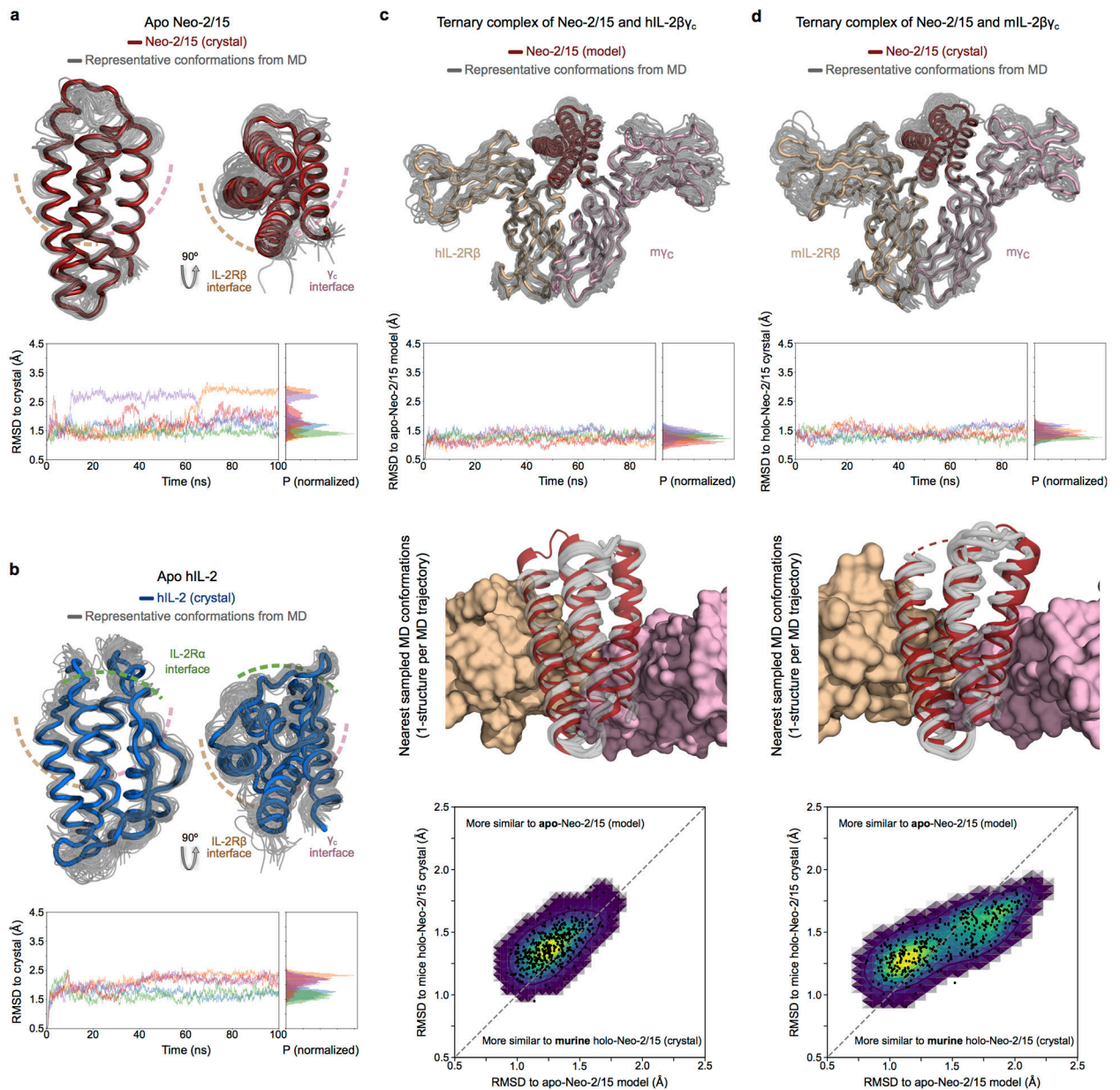
Figure E7. Conformational flexibility of Neo-2/15 in MD simulations.

a) MD simulations started from the computational model of Neo-2/15 *(top)* converged into structures similar to the crystal conformation. Apo-Neo-2/15 is shown in red thick tubes (chain A from PDBid: 6GD6) and 45 (randomly selected) MD conformations from 5-independent MD simulations are shown in thin grey tubes; *(bottom)* the plot shows the r.m.s.d.$_{C\alpha}$ along 5-independent MD simulations (avg r.m.s.d.$_{C\alpha}$= 1.93 Å); **b)** similar to "a)" but for (control) MD simulations started from the crystallographic structure of hIL-2. *(Top)* The crystal conformation of hIL-2 (chain A from PDBid: 2B5I) is shown in blue thick tubes and 45 (randomly selected) MD conformations from 5-independent simulations are shown in thin grey tubes (avg r.m.s.d.$_{C\alpha}$= 2.02 Å); **c)** *(top)* similar to "a-b" shows MD structures for simulations started from the computational model of Neo-2/15 bound to the hIL-2Rβɣ$_c$;

(middle-top) the plot shows the r.m.s.d.$_{C\alpha}$ along 5-independent MD simulations (avg r.m.s.d.$_{C\alpha}$ to apo-Neo-2/15 (model)= 1.28 Å); *(middle-bottom)* shows the nearest conformation (to the Apo-Neo-2/15 computational model) that were sampled on each of the 5-independent MD simulations performed (structures from the first 50ns of MD simulation were not considered); *(bottom)* shows a 2d-scatter plot (and the underlying density plot, where yellow, blue, green and purple colors represent decreasing densities) that compares the r.m.s.d.$_{C\alpha}$ (after discarding the first 50ns of MD simulation) for Apo-Neo-2/15 (computational model) *versus* the r.m.s.d.$_{C\alpha}$ for the holo-crystal structure of Neo-2/15 (in complex with the murine receptor). The conformations sampled by Neo-2/15 when in complex with the hIL-2Rβɣ$_c$ are more similar to the Apo-Neo-2/15 structure (computational model) than to the Neo-2/15 conformation observed in complex with the mIL-2Rβɣ$_c$ receptor. **d)** *(top, middle-top and middle-bottom)* analogous to "c)" but for MD simulations started from the computational model of Apo-Neo-2/15 in complex with the crystallographic structure of the mIL-2Rβɣ$_c$. The model of Apo-Neo-2/15 was initially placed by simply aligning (TMalign) the ternary computational model of Neo-2/15 with hIL-2Rβɣ$_c$ (from "c)") into the crystallographic structure of the mIL-2Rβɣ$_c$ (PDBid: 6GD5), avg r.m.s.d.$_{C\alpha}$ to holo-Neo-2/15 (murine) = 1.43 Å. *(bottom)* shows a 2d-scatter plot (and the underlying density plot, where yellow, blue, green and purple colors represent decreasing densities) that compares the r.m.s.d.$_{C\alpha}$ (after discarding the first 50ns of MD simulation) for Apo-Neo-2/15 (computational model) *versus* the r.m.s.d.$_{C\alpha}$ for the holo-crystal structure of Neo-2/15 (in complex with the murine receptor). Different to what is observed in "c)", the conformations sampled by Neo-2/15 when in complex with the mIL-2Rβɣ$_c$ are more similar to the Neo-2/15 conformation observed in the crystallographic structure of the ternary complex of Neo-2/15 with the mIL-2Rβɣ$_c$ receptor (see Figure 3). For clarity, all the r.m.s.d.$_{C\alpha}$ plots were filtered (running average filter, 5-frames = 100 ps), and the dots in the 2d scatter plots were subsampled every 25-conformations (i.e. 500 ps), however the density plot corresponds to all the conformations analyzed (i.e. the last 40ns × 5 MD simulations were analyzed, and conformations were recorded each 20ps).

Helix 1 consensus

Neoleukin-2/15   1 PKKKIQLHAEHALYDALMILNI 22
Interleukin-2   6 STKKTQLQLEHLLLDLQMILNG 27
Interleukin-15   1 ------NWVNVISDLKKIEDL 15

Helix 3 consensus

Neoleukin-2/15 34 LEDYAFNFELILEEIARLFESG 55
Interleukin-2   82 PRDLISNINVIVLELKGSETTF 103
Interleukin-15 59 IHDTVENLIILANNSLSSNGNV 80

Helix 2' consensus

Neoleukin-2/15 58 KDEAEKAKRMKEWMKRIKT 76
Interleukin-2   50 ATELKHLQCLEEELKPLEE 68
Interleukin-15 34 SCKVTAMKCFLLELQVISL 52

Helix 4 consensus

Neoleukin-2/15 80 EDEQEEMANAIITILQSWIFS 100
Interleukin-2 111 TATIVEFLNRWITFCQSIIST 131
Interleukin-15 93 EKNIKEFLQSFVHIVQMFINT 113

Figure E8. Overall sequence conservation in terms of binding for each of the 4-common helices combining the information from three different *de novo* designed IL-2 mimics.

The sequence logos (WebLogo) were generated using the combined data from in vitro binding experiments (against the heterodimeric mIL-2Rβγ$_c$, see Methods) from 3 independent SSM mutagenesis libraries for G2_neo2_40_1F_seq27, G2_neo2_40_1F_seq29 and G2_neo2_40_1F_seq36 (SI Figs. S8–10). All of these proteins are functional high-affinity mimetics of mice and human IL-2 (see SI Figures S6–11), some with different topologies than Neo-2/15, but all containing the four Helices H1, H3, H2' and H4. The logos show the combined information for each helix independently. Below each logo, a line graph shows the probability score (higher is more conserved) for each amino acid in the Neo-2/15 sequence. A red line in these line graphs highlights positions where the Neo-2/15 amino acid has a probability score 30% (i.e. these amino acids contribute more significantly to receptor binding as they are generally more enriched in the binding populations of all of the tested mimics). The helix represented by EACH logo is shown to the left of each logo in terms of its topological position in Neo-2/15. The sequences of the Neo-2/15 helices and those of the corresponding helices (structurally aligned) for natural hIL-2 (interleukin-2) and hIL-15 (interleukin-15) are shown below the graphs, demonstrating the unique character of Neo-2/15's helices and binding interfaces.

Table E1.

Characterization of several de novo designed mimics of IL-2/IL-15.

The table shows experimental and structural properties for several *de novo* IL-2/IL-15 mimics. hIL-2, mIL-2, and Super-2 are shown as references. The sequence similarity was calculated by structural alignment against hIL-2 (PDB ID: 2B5I) or mIL-2 (PDB ID: 4YQX). The EC50 field refers to pSTAT5 cell-signaling that was measured across six (6) independent experiments (denoted by the identifiers a–f in parentheses). "N/S" stands for nonsignificant and "N/A" for nonavailable. The binding and signaling experiments were performed 3 times with similar results..

	Binding affinity (Kd) to mIL-2R0Yc, and cell signaling In human NK (YT, CD25-) cells							
Name	Kd hIL-2RβYc (nM)	Kd HIL-2Rβ (nM)	EC50 (CD25-) pSTAT5p (nM) / (exp i.d.)	Seq identity to HIL-2 (% / (num a.a. algn))	Seq identity to mIL-2 (% / (num a.a. algn))	Exp. optimized	Parent molecule	a.a. length
hIL-2	*193.6*	*326.9*	*0.41 / (a)*	*100.0 / (120)*	*54.5/(112)*	-	-	133
mIL-2	*8034.0*	*4950.0*	*39.05 (a)*	*54.5/(112)*	*100/(122)*	-	-	130
Super-2 / Superkine (PDB: 3QAZ)	*300.9*	*2.0*	*0.07/(a)*	*94.9/(117)*	*50.9/(114)*	Y	*hIL-2*	133
G1_neo2_40	260.0	1457.0	0.14/(b)	47.7/(86)	30.4/(79)	N	-	87
G1_neo2_41	187.0	720.6	0.07 / (b)	47.7/(86)	30.4/(79)	N	-	87
G1_neo2_43	533.4	2861.0	0.21 / (b)	50.0/(86)	32.9/(79)	N	-	87
G1_neo2_40_1F	2.3	2.6	0.09/(c)	44.2/(86)	26.6/(79)	Y	G1_neo2_40	87
G2_neo2_40_1F_dsn36	113.9	27.6	0.12 / (a)	33.7/(89)	17.6/(85)	N	*De novo* mimetic design using template: G1 neo2 40 1F	100
Neoleukin-2/15 (G2_neo2_40_1F_dsn36)	**18.8**	**11.2**	**0.05 / (a)**	**29.2/(89)**	**15.7/(83)**	**Y**	**G2_neo2_40_1F_dsn36**	**100**

	Binding affinity (Kd) to mIL-2RβYc, and cell signaling (EC50) in murine T (CTLL-2, CD25+) cells							
Name	Kd mIL-2RβYc (nM)	Kd mIL-2Rβ (nM)	EC50 (CD25+) PSTAT5 (nM) / (exp i.d.)	Seq Identity to hIL-2 (% / (num a.a. algn))	Seq Identity to mIL-2 (% / (num a.a. algn))	Exp. optimized	Parent molecule	a.a. length
hIL-2	*492.2*	*8106.0*	*0.002/(d)*	*see previous table			
mIL-2	*126.2*	*1496.0*	*0.003/(e)*	*see previous table			
Super-2 / Superkine (PDB: 3QAZ)	*312.2*	*214.0*	*N/A*	*see previous table			
G1_neo2_40_1F	7.9	485.5	0.2 / (e)	*see previous table			
G1_neo2_40_1F_H1	2654.0	6799.0	37.38 / (d)	39.5/(86)	25.0 / (80)	Y	G1_neo2_40_1F	87
G1_neo2_40_1F_H2	963.7	68300.0	9.38 / (d)	40.7/(86)	26.2 / (80)	Y	G1_neo2_40_1F	87
G1_neo2_40_1F_H3	3828.0	N/S	35.2 / (d)	39.5/(86)	25.0 / (80)	Y	G1_neo2_40_1F	87

Binding affinity (Kd) to mIL-2R0Yc, and cell signaling In human NK (YT, CD25-) cells

Name	Kd hIL-2RβYc (nM)	Kd HIL-2Rβ (nM)	EC50 (CD25-) pSTAT5p (nM) / (exp i.d.)	Seq identity to HIL-2 (% / (num a.a. algn))	Seq identity to mIL-2 (% / (num a.a. algn))	Exp. optimized	Parent molecule	a.a. length
G1_neo2_40_1F_H4	391.8	10070.0	0.93 / (d)	41.9(86)	26.2 / (80)	Y	G1_neo2_40_1F	87
G1_neo2_40_1F_H5	5123.0	45300.0	84.69 / (d)	39.5(86)	23.8 / (80)	Y	G1_neo2_40_1F	87
G1_neo2_40_1F_M1	4.3	213.9	0.007/(d)	36.0(86)	25.0 / (80)	Y	G1_neo2_40_1F	87
G1_neo2_40_1F_M2	886.3	2599.0	3.11 /(d)	37.2 / (86)	25.0 / (80)	Y	G1_neo2_40_1F	87
G1_neo2_40_1F_M3	64.8	402.3	0.08/(d)	34.9(86)	25.3 / (79)	Y	G1_neo2_40_1F	87
G2_neo2_40_1F_seq04	80.0	N/A	1.95 1 (f)	38.4(86)	23.8 / (80)	N	Sequence redesign of G1_neo2_40_1F	87
G2_neo2_40_1F_seq12	39.1	N/A	1.74/(0	38.4(86)	25.3 / (79)	N	Sequence redesign of G1_neo2_40_1F	87
G2_neo2_40_1F_seq16	71.5	N/A	2.20/(f)	34.9(86)	22.5 / (80)	N	Sequence redesign of G1_neo2_40_1F	87
G2_neo2_40_1F_seq26	27.8	N/A	1.06/(0	39.5(86)	25.3 / (79)	N	Sequence redesign of G1_neo2_40_1F	87
G2_neo2_40_1F_seq27	13.6	N/A	0.24/(0	36.0(86)	25.0 / (80)	N	Sequence redesign of G1_neo2_40_1F	87
G2_neo2_40_1F_dsn29	38.2	N/A	0.48/(f)	36.6(82)	8.9 / (90)	N	*De novo* mimetic design using template: G1 neo2 40 1F	107
G2_neo2_40_1F_dsn30	925.0	N/A	7.61 /(f)	33.0/(97)	23.4 / (94)	N	*De novo* mimetic design using template: G1 neo2 40 1F	107
G2_neo2_40_1F_dsn36	568.5	2432.0	1.36 / (e)		*see previous table		*see previous table	
G2_neo2_40_1F_dsn40	69.2	N/A	0.50 1(f)	33.7 /(84)	17.9/(84)	N	*De novo* mimetic design using template: G1 neo2 40 1F	100
Neoleukin-2/15 (G2_neo2_40_1F_dsn36)	**38.4**	**16.1**	**0.07 / (e)**		*see previous table			

Table E2.

Crystallographic data table for (left) monomeric Neoleukin-2/15, and (right) the quaternary complex of Neoleukin-2/15 with mIL-2RβɣC.

Notes: *) Values in parentheses are for highest-resolution shell; a) Statistics are for data that were truncated by STARANISO to remove poorly measured reflections affected by anisotropy; b) The resolution limits for three directions in reciprocal space are indicated here. To accomplish this, STARANISO computed an ellipsoid post fitted by least squares to the cutoff surface, removing points where the fit was poor. Note that the cutoff surface is unlikely to be perfectly ellipsoidal, so this is only an estimate; c) The anisotropic completeness was obtained by least squares fitting an ellipsoid to the reciprocal lattice points at the cutoff surface defined by a local mean I/σI threshold of 1.0, rejecting outliers in the fit due to spurious deviations (including any cusp), and calculating the fraction of observed data lying inside the ellipsoid so defined. Note that the cutoff surface is unlikely to be perfectly ellipsoidal, so this is only an estimate..

	Neoleukin-2/15 (6DG6)	Neoleukin-2/15 ternary complex with mIL-2RβɣC (6DG5)
Data collection		
Space group	P 21 21 21	P 21 2 21
Cell dimensions		
a, b, c (Å)	73.73,86.8, 92.31	65.125, 67.914, 172.084
α,β,ɣ (°)	90, 90, 90	90, 90 ,90
Resolution (Å)	39.28 – 1.999(2.07 – 1.999)*	47.005–2.516(2.828–2.516)
Ellipsoidal[a] resolution limit (Å)	-	3.422 (a*)
(direction)[b]	-	2.407 (b*)
	-	3.475 (c*)
R_{sym}	0.1027(1.709)	0.3590(2.516)
I/cI	12.19(1.25)	6.8 (1.3)
Completeness (%)	92.58 (77.83)	52.3 (9.0)
Completeness (ellipsoidal)[c] (%)		93.2 (77.2)
Redundancy	8.7 (8.1)	9.5(11.2)
Refinement		
Resolution (Å)	39.28 – 1.999(2.07 – 1.999)	47.005–2.516
No. reflections	37747(3125)	13923 (136)
R_{work} / R_{free}	0.2037/0.2260	0.2211/0.2658
No. atoms	4791	4100
Protein	4735	3949
Ligand/ion	0	138
Water	56	13
B-factors	52.56	47.05
Protein	52.54	46.39
Ligand/ion	-	67.79

	Neoleukin-2/15 (6DG6)	Neoleukin-2/15 ternary complex with mIL-2RβΥc (6DG5)
Water	54.21	27.31
R.m.s. deviations		
Bond lengths (Å)	0.005	0.004
Bond angles (°)	0.88	0.94

Supplementary Material

Refer to Web version on PubMed Central for supplementary material.

Acknowledgements:

References

1. Akdis M et al. Interleukins, from 1 to 37, and interferon-γ: receptors, functions, and roles in diseases. J. Allergy Clin. Immunol 127, 701–21.e1–70 (2011). [PubMed: 21377040]

2. Smyth MJ, Cretney E, Kershaw MH & Hayakawa Y Cytokines in cancer immunity and immunotherapy. Immunol. Rev 202, 275–293 (2004). [PubMed: 15546400]

3. Lotze MT et al. In vivo administration of purified human interleukin 2. II. Half life, immunologic effects, and expansion of peripheral lymphoid cells in vivo with recombinant IL 2. J. Immunol 135, 2865–2875 (1985). [PubMed: 2993418]

4. Moraga I et al. Synthekines are surrogate cytokine and growth factor agonists that compel signaling through non-natural receptor dimers. Elife 6, (2017).

5. Vazquez-Lombardi R et al. Potent antitumour activity of interleukin-2-Fc fusion proteins requires Fc-mediated depletion of regulatory T-cells. Nat. Commun 8, 15373 (2017). [PubMed: 28497796]

6. Sockolosky JT et al. Selective targeting of engineered T cells using orthogonal IL-2 cytokine-receptor complexes. Science 359, 1037–1042 (2018). [PubMed: 29496879]

7. Kureshi R, Bahri M & Spangler JB Reprogramming immune proteins as therapeutics using molecular engineering. Curr. Opin. Chem. Eng 19, 27–34 (2018).

8. Levin AM et al. Exploiting a natural conformational switch to engineer an interleukin-2 'superkine'. Nature 484, 529–533 (2012). [PubMed: 22446627]

9. Sarkar CA et al. Rational cytokine design for increased lifetime and enhanced potency using pH-activated 'histidine switching'. Nat. Biotechnol 20, 908–913 (2002). [PubMed: 12161759]

10. Spangler JB, Moraga I, Mendoza JL & Garcia KC Insights into cytokine-receptor interactions from cytokine engineering. Annu. Rev. Immunol 33, 139–167 (2015). [PubMed: 25493332]

11. Charych DH et al. NKTR-214, an Engineered Cytokine with Biased IL2 Receptor Binding, Increased Tumor Exposure, and Marked Efficacy in Mouse Tumor Models. Clin. Cancer Res 22, 680–690 (2016). [PubMed: 26832745]

12. Dougan M et al. Targeting Cytokine Therapy to the Pancreatic Tumor Microenvironment Using PD-L1-Specific VHHs. Cancer Immunol Res 6, 389–401 (2018). [PubMed: 29459478]

13. Tzeng A, Kwan BH, Opel CF, Navaratna T & Dane Wittrup K Antigen specificity can be irrelevant to immunocytokine efficacy and biodistribution. Proceedings of the National Academy of Sciences 112, 3320–3325 (2015).

14. Zhu EF et al. Synergistic innate and adaptive immune response to combination immunotherapy with anti-tumor antigen antibodies and extended serum half-life IL-2. Cancer Cell 27, 489–501 (2015). [PubMed: 25873172]

15. Kim DE, Gu H & Baker D The sequences of small proteins are not extensively optimized for rapid folding by natural selection. Proceedings of the National Academy of Sciences 95, 4982–4986 (1998).

16. Taverna DM & Goldstein RA Why are proteins marginally stable? Proteins 46, 105–109 (2002). [PubMed: 11746707]

17. Foit L et al. Optimizing Protein Stability In Vivo. Mol. Cell 36, 861–871 (2009). [PubMed: 20005848]

18. Marshall SA, Lazar GA, Chirino AJ & Desjarlais JR Rational design and engineering of therapeutic proteins. Drug Discov. Today 8, 212–221 (2003). [PubMed: 12634013]

19. De Groot AS & Scott DW Immunogenicity of protein therapeutics. Trends Immunol 28, 482–490 (2007). [PubMed: 17964218]

20. Peyvandi F et al. A Randomized Trial of Factor VIII and Neutralizing Antibodies in Hemophilia A. N. Engl. J. Med 374, 2054–2064 (2016). [PubMed: 27223147]

21. Antonelli G, Currenti M, Turriziani O & Dianzani F Neutralizing antibodies to interferon-alpha: relative frequency in patients treated with different interferon preparations. J. Infect. Dis 163, 882–885 (1991). [PubMed: 1901335]

22. Eckardt K-U & Casadevall N Pure red-cell aplasia due to anti-erythropoietin antibodies. Nephrol. Dial. Transplant 18, 865–869 (2003). [PubMed: 12686654]

23. Prümmer O Treatment-induced antibodies to interleukin-2. Biotherapy 10, 15–24 (1997). [PubMed: 9261546]

24. Fineberg SE et al. Immunological responses to exogenous insulin. Endocr. Rev 28, 625–652 (2007). [PubMed: 17785428]

25. Boyman O & Sprent J The role of interleukin-2 during homeostasis and activation of the immune system. Nat. Rev. Immunol 12, 180–190 (2012). [PubMed: 22343569]

26. Blattman JN et al. Therapeutic use of IL-2 to enhance antiviral T-cell responses in vivo. Nat. Med 9, 540–547 (2003). [PubMed: 12692546]

27. Siegel JP & Puri RK Interleukin-2 toxicity. J. Clin. Oncol 9, 694–704 (1991). [PubMed: 2066765]

28. Mott HR et al. The solution structure of the F42A mutant of human interleukin 2. J. Mol. Biol 247, 979–994 (1995). [PubMed: 7723044]

29. Carmenate T et al. Human IL-2 mutein with higher antitumor efficacy than wild type IL-2. J. Immunol 190, 6230–6238 (2013). [PubMed: 23677467]

30. Tagaya Y, Bamford RN, DeFilippis AP & Waldmann TA IL-15: a pleiotropic cytokine with diverse receptor/signaling pathways whose expression is controlled at multiple levels. Immunity 4, 329–336 (1996). [PubMed: 8612127]

31. Ozaki K & Leonard WJ Cytokine and cytokine receptor pleiotropy and redundancy. J. Biol. Chem 277, 29355–29358 (2002). [PubMed: 12072446]

32. Lin JX et al. The role of shared receptor motifs and common Stat proteins in the generation of cytokine pleiotropy and redundancy by IL-2, IL-4, IL-7, IL-13, and IL-15. Immunity 2, 331–339 (1995). [PubMed: 7719938]

33. Ma A, Boone DL & Lodolce JP The pleiotropic functions of interleukin 15: not so interleukin 2-like after all. J. Exp. Med 191, 753–756 (2000). [PubMed: 10704456]

34. Procko E et al. A computationally designed inhibitor of an Epstein-Barr viral Bcl-2 protein induces apoptosis in infected cells. Cell 157, 1644–1656 (2014). [PubMed: 24949974]

35. Chevalier A et al. Massively parallel de novo protein design for targeted therapeutics. Nature 550, 74–79 (2017). [PubMed: 28953867]

36. Jacobs TM et al. Design of structurally distinct proteins using strategies inspired by evolution. Science 352, 687–690 (2016). [PubMed: 27151863]

37. Correia BE et al. Proof of principle for epitope-focused vaccine design. Nature 507, 201–206 (2014). [PubMed: 24499818]

38. Boyken SE et al. De novo design of protein homo-oligomers with modular hydrogen-bond network-mediated specificity. Science 352, 680–687 (2016). [PubMed: 27151862]

39. Ring AM et al. Mechanistic and structural insight into the functional dichotomy between IL-2 and IL-15. Nat. Immunol 13, 1187–1195 (2012). [PubMed: 23104097]

40. Fleishman SJ et al. RosettaScripts: a scripting language interface to the Rosetta macromolecular modeling suite. PLoS One 6, e20161 (2011). [PubMed: 21731610]

41. Leaver-Fay A et al. Rosetta3. in Methods in Enzymology 545–574 (2011).

42. Chaudhury S, Lyskov S & Gray JJ PyRosetta: a script-based interface for implementing molecular modeling algorithms using Rosetta. Bioinformatics 26, 689–691 (2010). [PubMed: 20061306]

43. Wang X, Rickert M & Garcia KC Structure of the quaternary complex of interleukin-2 with its alpha, beta, and gammac receptors. Science 310, 1159–1163 (2005). [PubMed: 16293754]

44. Robinson TO & Schluns KS The potential and promise of IL-15 in immuno-oncogenic therapies. Immunol. Lett 190, 159–168 (2017). [PubMed: 28823521]

45. Bouchaud G et al. The Exon-3-Encoded Domain of IL-15Rα Contributes to IL-15 High-Affinity Binding and Is Crucial for the IL-15 Antagonistic Effect of Soluble IL-15Rα. J. Mol. Biol 382, 1–12 (2008). [PubMed: 18656487]

46. Cao X Regulatory T cells and immune tolerance to tumors. Immunol. Res 46, 79–93 (2009).

47. Fontenot JD, Rasmussen JP, Gavin MA & Rudensky AY A function for interleukin 2 in Foxp3-expressing regulatory T cells. Nat. Immunol 6, 1142–1151 (2005). [PubMed: 16227984]

48. Chen X et al. Combination therapy of an IL-15 superagonist complex, ALT-803, and a tumor targeting monoclonal antibody promotes direct antitumor activity and protective vaccinal effect in a syngenic mouse melanoma model. J Immunother Cancer 3, P347 (2015).

49. Dougan M & Dranoff G Immune Therapy for Cancer. Annu. Rev. Immunol 27, 83–117 (2009). [PubMed: 19007331]

50. Roberts MJ, Bentley MD & Harris JM Chemistry for peptide and protein PEGylation. Adv. Drug Deliv. Rev 64, 116–127 (2012).

Methods References

51. Fleishman SJ et al. Computational design of proteins targeting the conserved stem region of influenza hemagglutinin. Science 332, 816–821 (2011). [PubMed: 21566186]

52. Chang HC et al. A general method for facilitating heterodimeric pairing between two proteins: application to expression of alpha and beta T-cell receptor extracellular segments. Proc. Natl. Acad. Sci. U. S. A 91, 11408–11412 (1994). [PubMed: 7972074]

53. Yodoi J et al. TCGF (IL 2)-receptor inducing factor(s). I. Regulation of IL 2 receptor on a natural killer-like cell line (YT cells). J. Immunol 134, 1623–1630 (1985). [PubMed: 2578514]

54. Kuziel WA, Ju G, Grdina TA & Greene WC Unexpected effects of the IL-2 receptor alpha subunit on high affinity IL-2 receptor assembly and function detected with a mutant IL-2 analog. J. Immunol 150, 3357–3365 (1993). [PubMed: 8468475]

55. Silva D-A, Stewart L, Lam K-H, Jin R & Baker D Structures and disulfide cross-linking of de novo designed therapeutic mini-proteins. FEBS J (2018). doi:10.1111/febs.14394

56. Stumpp MT, Kaspar Binz H & Amstutz P DARPins: A new generation of protein therapeutics. Drug Discov. Today 13, 695–701 (2008). [PubMed: 18621567]

57. Marcos E & Silva D-A Essentials of de novo protein design: Methods and applications. Wiley Interdiscip. Rev. Comput. Mol. Sci e1374 (2018).

58. Berger S et al. Computationally designed high specificity inhibitors delineate the roles of BCL2 family proteins in cancer. Elife 5, (2016).

59. Abraham MJ et al. GROMACS: High performance molecular simulations through multi-level parallelism from laptops to supercomputers. SoftwareX 1–2, 19–25 (2015).

60. Markidis S & Laure E Solving Software Challenges for Exascale: International Conference on Exascale Applications and Software, EASC 2014, Stockholm, Sweden, April 2–3, 2014, Revised Selected Papers. (Springer, 2015).

61. Lindorff-Larsen K et al. Improved side-chain torsion potentials for the Amber ff99SB protein force field. Proteins 78, 1950–1958 (2010). [PubMed: 20408171]

62. Leszczynski J & Shukla MK Practical Aspects of Computational Chemistry: Methods, Concepts and Applications. (Springer Science & Business Media, 2009).

63. Berendsen HJC, Postma JPM, van Gunsteren WF, DiNola A & Haak JR Molecular dynamics with coupling to an external bath. J. Chem. Phys 81, 3684–3690 (1984).

64. Parrinello M & Rahman A Polymorphic transitions in single crystals: A new molecular dynamics method. J. Appl. Phys 52, 7182–7190 (1981).

65. Essmann U et al. A smooth particle mesh Ewald method. J. Chem. Phys 103, 8577–8593 (1995).

66. Páll S & Hess B A flexible algorithm for calculating pair interactions on SIMD architectures. Comput. Phys. Commun 184, 2641–2650 (2013).

67. Welcome to Python.org. Python.org Available at: https://www.python.org/. (Accessed: 29th May 2018)

68. Perez F & Granger BE IPython: A System for Interactive Scientific Computing. Comput. Sci. Eng 9, 21–29 (2007).

69. Oliphant TE Python for Scientific Computing. Comput. Sci. Eng 9, 10–20 (2007).

70. Oliphant TE A Guide to NumPy. (2006).

71. Hunter JD Matplotlib: A 2D Graphics Environment. Comput. Sci. Eng 9, 90–95 (2007).

72. Garreta R & Moncecchi G Learning scikit-learn: Machine Learning in Python. (Packt Publishing Ltd, 2013).

73. Behnel S et al. Cython: The Best of Both Worlds. Comput. Sci. Eng 13, 31–39 (2011).

74. McKinney W Python for Data Analysis: Data Wrangling with Pandas, NumPy, and IPython. ('O'Reilly Media, Inc.', 2017).

75. PyMOL | pymol.org. Available at: https://pymol.org/2/. (Accessed: 30th May 2018)

76. Minami S, Sawada K & Chikenji G MICAN: a protein structure alignment algorithm that can handle Multiple-chains, Inverse alignments, C(α) only models, Alternative alignments, and Non-sequential alignments. BMC Bioinformatics 14, 24 (2013). [PubMed: 23331634]

77. Crooks GE, Hon G, Chandonia J-M & Brenner SE WebLogo: a sequence logo generator. Genome Res 14, 1188–1190 (2004). [PubMed: 15173120]
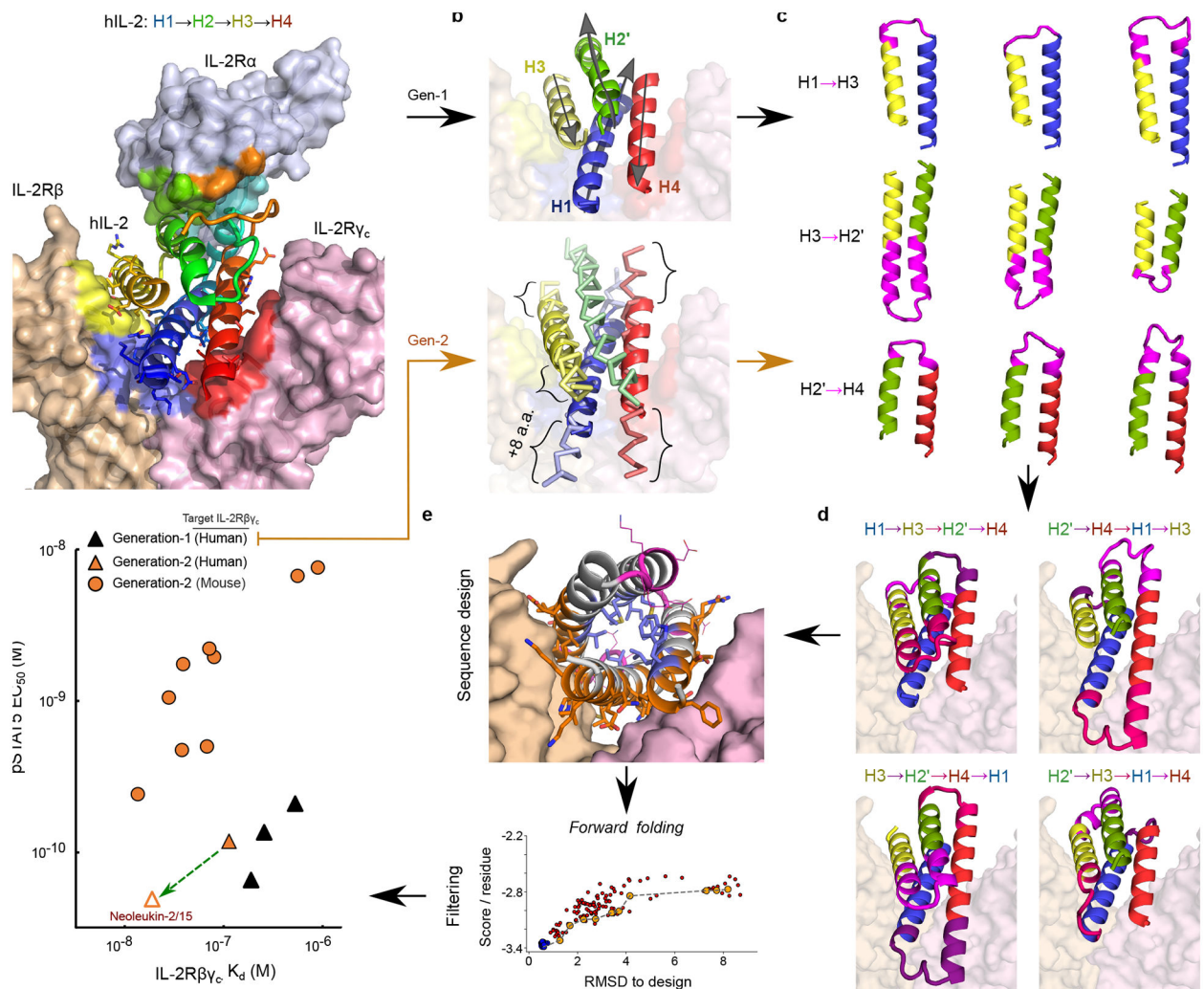
Figure 1. Computational design of *de novo* cytokine mimics.
a) Structure of hIL-2 (cartoon representation) in complex with the hIL-2Rαβɣc (surface representation) (PDB ID: 2B5I), **b)** The designed mimics have four helices; three (blue, yellow and red) mimic IL-2 interactions with hIL-2Rβɣc, while the fourth (green) holds the first three in place. Top-first generation: each of the core elements of IL-2 (helices H1-H4) were independently idealized using fragment-assembly from a clustered ideal 4 residue fragment database; bottom-second generation: the core elements were built using parametric equations that recapitulate the shape of each disembodied helix, allowing changes in the length of each helix by +/− 8 a.a. ; **c)** Pairs of helices were reconnected using ideal loop fragments, representative examples are shown with the newly built elements connecting each pair of helices in magenta; **d)** Combination of helix hairpins in **(c)** to generate fully connected protein backbones; **e)** Rosetta flexible backbone sequence design. **f)** Binding and activity of selected designs (solid symbols), the green arrow originates at the parent of Neo2–15. (see Table E1).
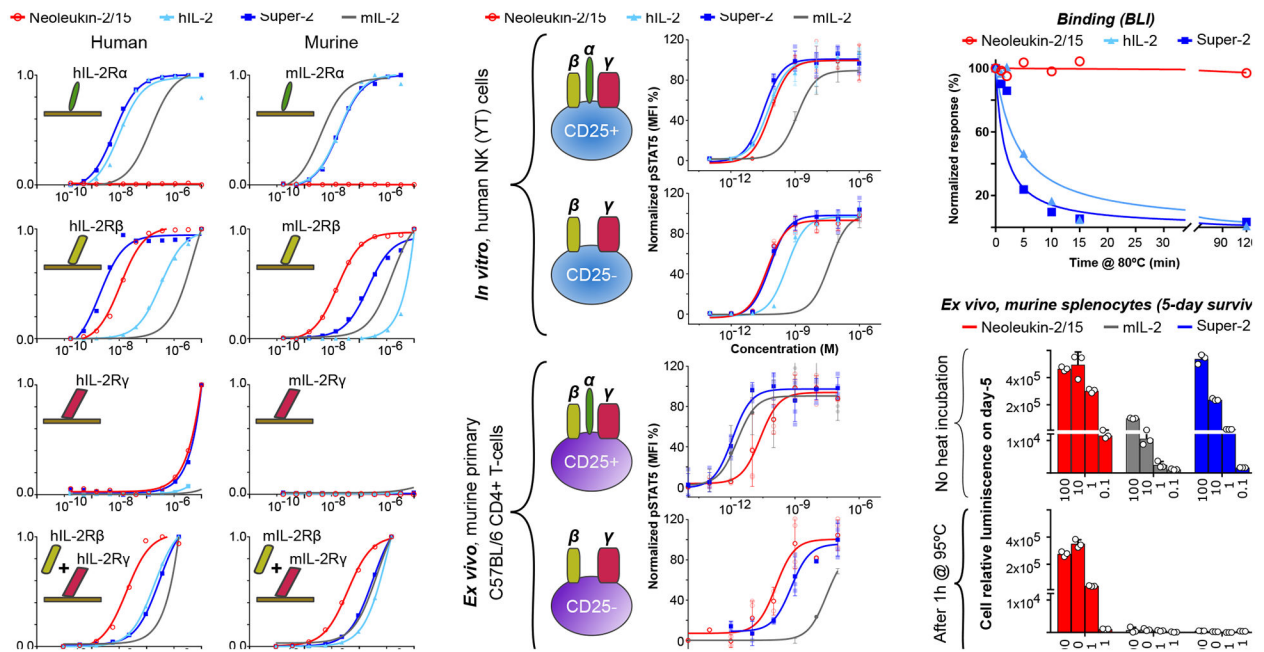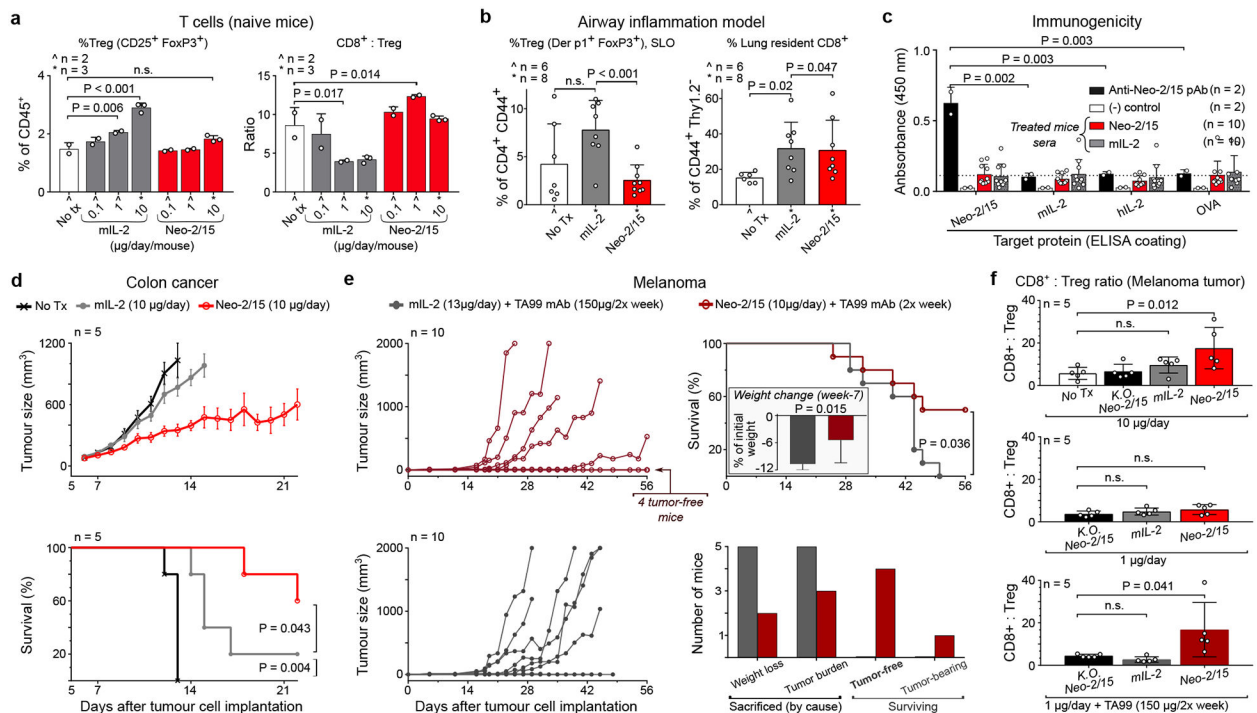
Figure 2. Characterization of Neo-2/15.
a) Receptor subunit binding assessed by SPR: Neoleukin-2–15 (red) does not bind IL-2Rα (top row), but binds more tightly than IL-2 (light blue) and Super-2 (dark blue) to IL-2β (second row) and IL-2βγ_c (bottom row) (K_d values in extended table E1; experiments performed 3 times with similar results); **b)** Neoleukin-2/15 stimulates STAT5 phosphorylation more potently than IL-2 in cells expressing IL2Rbg but not IL2Ra (CD25-) in both (in vitro) human NK, (n=3; experiments performed 3 times with similar results) and murine CD4^{+} T cells (n=4; data is from a pool of 3 independent experiments). c) <u>Top</u>: Neo-2/15 can be incubated for 2 hours at 80°C without loss of binding against hIL-2Rβγ_c, whereas hIL-2 and Super-2 quickly lose activity (immobilized hIL-2Rγ_c with in-solution hIL-2Rβ at 500 nM; experiment performed once); <u>Bottom</u>: Following incubation at 95°C for 1 hour, Neo-2/15 still drives cell survival effectively (with ~70% luminescence remaining at 10 ng/ml relative to cells treated with non-heat incubated Neo 2/15), whereas mIL2 and Super-2 are inactivated (n=3; experiment performed 3 times with similar results). In all plots, the whiskers represent ∓1-standard deviation and are centered in the mean.
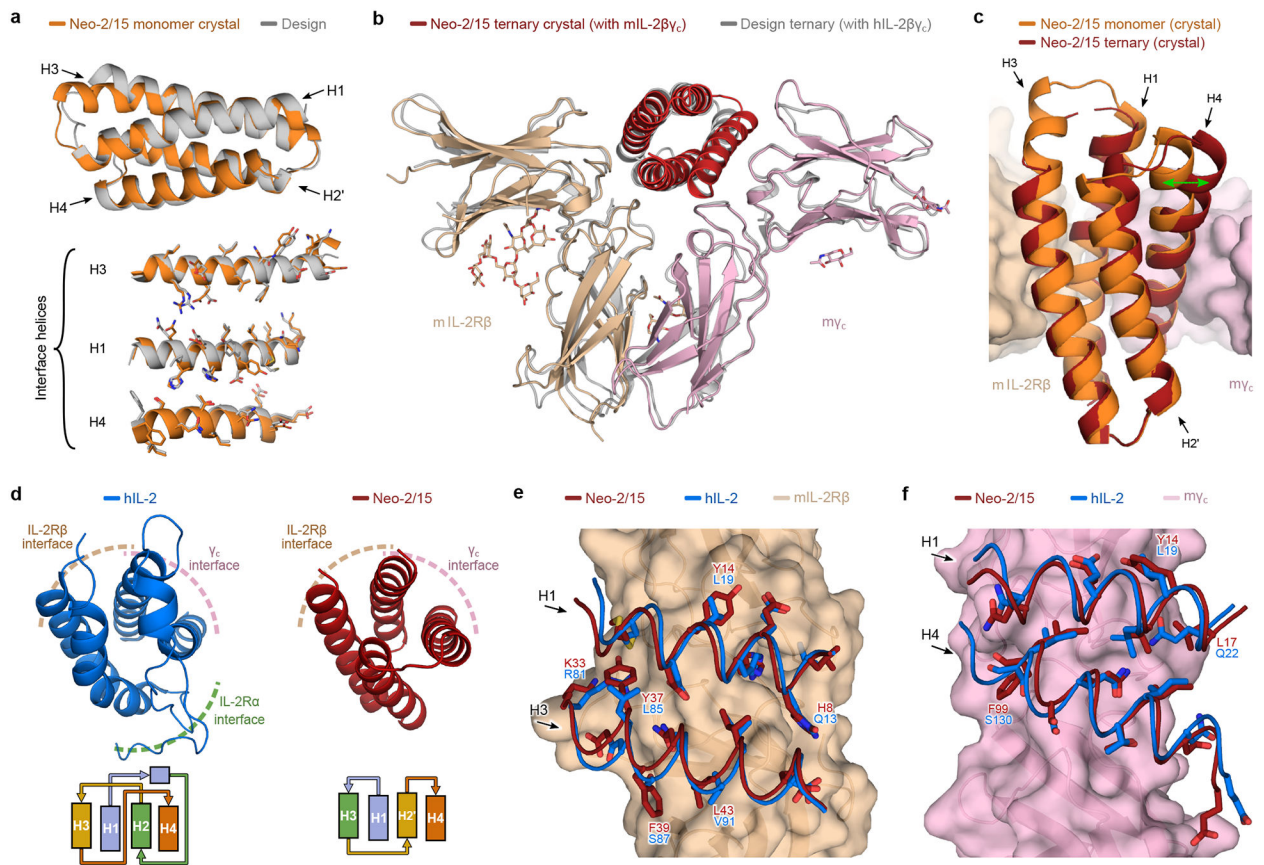
Figure 3. Structure of Neo-2/15 and its ternary complex with mIL-2Rβγ$_c$.
a) <u>Top</u>: structural alignment of Neo-2/15 chain A (orange) with the design model (grey, r.m.s.d 1.11 Å for 100 Cα atoms); <u>Bottom</u>: detail of interface helices H1, H3 and H4 (numbered according to hIL-2, Fig. 1). The interface side chains are shown in sticks ; **b)** crystal structure of the ternary complex of Neo-2/15 (red) with mIL-2Rβ (wheat) and γ$_c$ (pink), aligned to the design model against hIL-2Rβγ$_c$ (grey, r.m.s.d 1.27 Å for the 93 modeled Cα atoms of Neo-2/15 in the ternary complex); **c)** structural alignment of monomeric Neo-2/15 (chain A, orange) with Neo-2/15 in the ternary complex (red, r.m.s.d 1.71 Å for the 93 modeled Cα atoms in the ternary complex), highlighting an ~4.0 Å shift of helix H4 in the ternary-complex structure compared to the monomeric crystal structure (green double-headed arrow); **d)** comparison of the crystallographic structures of <u>left</u>: hIL-2 (cartoon representation in blue) and <u>right</u>: Neo-2/15 from the ternary complex in "b)" (cartoon representation in red). The regions that interact with the IL-2Rβ and γ$_c$ are indicated. Topology diagrams are at the bottom. The loop-rich region from hIL-2 that interacts with hIL-2Rα does not exist in the *de novo* mimic Neo-2/15. ; **e-f)** comparison of the binding interfaces of Neo-2/15 and hIL-2 with mIL-2Rβ and mIL-2Rγ$_c$, respectively. Interfacial amino acids are shown as sticks, and those that differ between hIL-2 and Neo-2/15 are denoted with labels.

Figure 4. In vivo characterization of Neo-2/15.
a) mIL-2 but not Neo-2/15 enhances CD4+ Treg expansion in naive mice T cells; **b)** In a mice airway inflammation model (20 μg/day/mouse, 7 days), Neo-2/15 does not increase the frequency of antigen-specific CD4+ Foxp3+ T_{regs} in the lymphoid organs (SLO). **c)** Neo-2/15 does not have detectable immunogenicity. Mice were immunized with Neo-2/15 (red) or mIL-2 (grey) (14 days of daily i.p. injection, 10 μg/day), IgG was detected by ELISA. Anti-Neo-2/15 pAb was used as a positive control and did not cross-react with mIL-2 or hIL2; **d)** Neo-2/15 is more effective than mIL-2 in a colorectal cancer model (CT26). Starting on day 6, mice were i.p. treated daily with mIL-2 or Neo-2/15 (10 μg), or were left untreated. Tumor growth curves (*top*) show only surviving mice and stop if a group fell below 50% of the initial n. Survival curves (*bottom*). Mice were euthanized if weight loss exceeded 10%, or tumor size reached 1000 mm³; **e)** In a melanoma model (B16F10), combination of mAb TA99 with Neo-2/15 is more effective than with mIL-2. Starting on day 1, mice were i.p. treated daily with Neo-2/15 (10 μg) or equimolar mIL-2. Twice-weekly treatment with TA99 added on day 3. Tumor growth curves (*left*). Survival curve (top right), inset shows average weight change. Quantification of the cause of death (*bottom right*). f) Neo2/15 elicits a higher CD8+ : Treg ratio than mIL-2. Whiskers are ∓1-standard deviation centered on the mean, except in growth curves they are ∓1-standard error of the mean. Results analyzed by one-way ANOVA (95% confidence interval), except survival curves were assessed using the Mantel-cox test (95% confidence interval). All experiments were performed twice with similar results, except b) shows data pooled from 3 independent experiments.